Erzeugung von Zwei-Farben-Polarisationsverschränkung mit einem nichtlinearen Kristall in *Folded Sandwich* Geometrie

DIPLOMARBEIT

zur Erlangung des akademischen Grades
Diplom
im Fach Physik

eingereicht an der
Mathematisch-Naturwissenschaftlichen Fakultät
Institut für Physik
Humboldt-Universität zu Berlin

von
Herrn Thomas Kreißl
geboren am 21.08.1980 in Erlangen

Betreuung:

1. *Prof. Dr. Oliver Benson*
2. *Prof. Achim Peters Ph.D.*

eingereicht am: *31. März 2015*

Abbreviations

Abbreviation	Explanation
APD	Avalanche photodiode
BDCZ	Briegel, Dür, Cirac, Zoller
BK7	Standard optical glass
CH	Clauser, Horne
CHSH	Clauser, Horne, Shimony, Holt
cps	counts per second
EPR	Einstein, Podolsky and Rosen
DFG	Difference frequency generation
MgO:PPLN	Periodically poled lithium niobate doped with magnesium oxid
OPO	Optical parametric oscillator
SFG	Sum frequency generation
SHG	Second harmonic generation
SPDC	Spontaneous parametric down-conversion
SSPD	Superconducting single photon detector
YVO4	Yttrium ortho vanadate

Abstract

Entanglement, a property of quantum systems, is a fundamental resource in the field of quantum information. For testing quantum theory as well as for experiments in quantum computation or quantum communication it is an important resource in experiments. Experiments as the violation of Bell's inequality [CS78], quantum teleportation [UTSM+07], entanglement swapping [PBWZ98] or quantum logic gates [OFV09] need high-fidelity entangled input states. Also of great interest is the distribution of entanglement over long distances, since an amplification of quantum information is not possible due to the no-cloning theorem [WZ82].
For the distribution of entanglement in optical networks the flying qubits need to match the telecom band at 1.5 µm, or alternatively with higher losses at 1.3 µm. To date, high quality quantum dots with emission at the telecom wavelength are not available. By using high quality quantum dots at 900 nm the future goal is to convert the quantum information of a quantum dot photon to a photon at the telecom band. This requires a two-color polarization-entangled photon pair source acting as a teleportation interface.
In the frame of this work, a novel scheme called the two-color, folded sandwich [SRJ+13] combines advantages of the Sagnac and the crossed crystal configuration. In the folded sandwich scheme, also called linearly double pass, only one down-conversion crystal is implemented, together with a wavelength-independent rotation of polarization.
In this work, the rotation is implemented using a Fresnel rhomb instead of an achromatic quarter wave plate. The spectral properties and the simultaneous creation have been observed, as well as the tunability of the source with respect to the generated wavelengths. Furthermore, entanglement was detected in the polarization state of the photon pairs.

Zusammenfassung

Verschränkung, eine Eigenschaft von Quantensystemen, ist eine fundamentale Resource im Gebiet der Quanteninformation. Zum Test der Quantentheorie als auch für Experimente in der Quanteninformation und der Quantenkommunikation ist sie eine wichtige Resource für Experimente und zukünftige Anwendungen. Experimente wie die Verletzung der Bellschen Ungleichung [CS78], der Quantenteleportation [UTSM+07], dem Verschränkungsaustausch [PBWZ98] oder der logischen Quantengatter [OFV09] benötigen verschränkte Zustände. Von großem Interesse ist die Verbreitung von Verschränkung über große Distanzen, da eine Verstärkung der Quanteninformation aufgrund des no-cloning theorems [WZ82] nicht möglich ist. In optischen Netzwerken wird standardmäßig im 1.5 µm oder mit größeren Verlusten im 1.3 µm Bereich kommuniziert. Da hochqualitative Quantenpunkte aktuell nur im Bereich von 900 nm emittieren wird eine Schnittstelle benötigt, um die Quanteninformation des stationären Qubits auf die fliegenden Qubits im Transmissionbereich optischer Glasfasernetzwerke zu übertragen. Im Rahmen dieser Arbeit wurde eine neuartige Quelle zweifarbiger polarisationsverschränkter Photonenpaare aufgebaut [SRJ+13]. Der Folded Sandwich Aufbau benötigt zur Erzeugung der Verschränkung nur einen nichtlinearen optischen Kristall zusammen mit einer wellenlängenunabhängigen Rotation der Polarisation. In dieser Arbeit wurde an Stelle eines achromatischen $\lambda/4$-Plättchens ein Fresnelsches Parallelepiped zur Rotation der Polarisation der beteiligten Wellen verwendet. Es wurden die spektralen Eigenschaften der Quelle sowie die Verstimmung der Wellenlängen hinsichtlich zukünftiger Anwendungen untersucht. Darüberhinaus wurde Verschränkung im Polarisationszustand der Photonenpaare detektiert.

Contents

1 Introduction **2**

2 Principles **5**
2.1 Nonlinear Optics . . . 5
2.1.1 Phase Matching . . . 7
2.1.2 Nonlinear Optics with Focused Gaussian Beams . . . 8
2.1.3 Spontaneous Parametric Down-Conversion . . . 9
2.2 Quantum Information . . . 10
2.2.1 Qubits . . . 10
2.2.2 Entangled states . . . 13
2.2.3 Einstein, Podolsky and Rosen . . . 14
2.2.4 Bell Inequalities . . . 15
2.2.5 Entanglement measures . . . 17

3 Experimental Setup **22**
3.1 Two-color Folded Sandwich . . . 22
3.1.1 Linear double pass scheme . . . 22
3.1.2 Down-Conversion in periodically poled lithium niobate . . . 26
3.1.3 Fresnel Rhomb . . . 28
3.1.4 Phase Compensation . . . 30
3.2 Filtering quantum light with a Czerny-Turner spectrograph . . . 34
3.3 Single Mode Coupling . . . 38
3.4 Detectors . . . 40
3.4.1 Single-photon avalanche diode . . . 40
3.4.2 Superconducting single photon detector . . . 41
3.5 Gated coincidence measurements . . . 41
3.6 Tuning of the relative phase using a crystal oven . . . 42
3.7 Polarization correlations . . . 43

4 Results **48**
4.1 Folded Sandwich . . . 48
4.2 Spontaneous parametric down-conversion . . . 50
4.2.1 Spectral Width of Photon Pairs . . . 52
4.2.2 Tunability . . . 52
4.2.3 Brightness . . . 55
4.3 Photon Pair generation . . . 56

4.4 Single mode coupling . . . 59
4.5 Entanglement detection . . . 60
4.6 Discussion . . . 62

5 Outlook **63**

A Refractive indexes / Sellmeier equations **69**
A.1 Refractive Index of BK7 . . . 69
A.2 Refractive Index of YVO4 . . . 70
A.2.1 Foctek Photonics . . . 70
A.2.2 Sato . . . 70
A.2.3 Zelmon . . . 71
A.3 Refractive index of MgO:PPLN . . . 72

B Statistical Error **73**
B.1 Visibility . . . 73
B.2 Bell-state Fidelity . . . 73
B.3 Entanglement Witness . . . 73

1 Introduction

In 1935 Albert Einstein, Boris Podolsky and Nathan Rosen (EPR) who in their paper [EPR35] used the extra-ordinary properties of two-particle quantum states to point out that the formalism of quantum mechanics may be incomplete. Soon after, Schrödinger called this feature of compound quantum states with the word "Verschränkung". 30 years later, it was John Bell who came up with a experimentally testable inequality, the Bell inequality [Bel64]. He reopened the formerly philosophical debate over whether there may be hidden variables in quantum mechanics. His inequality, later improved by Clauser, Horn, Shimony and Holt (CHSH) [CHSH69], was able to rule out theories containing local hidden variables.
The first series [FC72, Cla76, FT76] of Bell tests in the 1970s used photon pairs entangled in their polarization degree of freedom, emitted in certain atomic cascades. One of the first experiments with a strong violation of Bell's inequality was realized by Aspect [AGR81, ADR82] in Paris. With the development of laser physics and nonlinear optics it was then possible to build more efficient sources of polarization-entangled photon pairs based on nonlinear optical effects [KMW$^+$95, Kwi99]. Now, it was possible to control the direction of the emission and thus to efficiently couple the entangled pair of photons into optical fibers [FHP$^+$07, LT05, TW08, LTMP06]. All these experiments confirm the violation of Bell's inequalities and give rise to extraordinary properties of entangled quantum states.
A number of experiments showed that entangled photons are not only subject to experiments regarding the nature of physical reality, but can also find applications in quantum communication, namely quantum teleportation [UTSM$^+$07, JRY$^+$10]. By making use of quantum teleportation which is the possibility to teleport an unknown quantum state from a sender Alice to a long distant receiver Bob, it is possible to distribute entanglement over large distances. In quantum communication it is thus essential to be able to distribute entangled quantum states over long distances. However, todays fibers restrict quantum communication to distances of several 100 km.
The quantum repeater scheme is beating the loss in optical fibers, decoherence and the impossibility to re-amplify quantum information due to the no-cloning theorem [WZ82]. Quantum repeaters [BDCZ98, BPM$^+$97] may allow quantum communication on a global scale.
In Fig. 1.1 the BDCZ [BDCZ98] scheme is depicted, representing a quantum repeater scheme. The photons of the entangled pairs are only traveling along a fraction of the whole distance of transmission. In order to transmit the entanglement, a joint measurement of two photons is performed, where each of the two photons belongs to a different entangled photon pair. This process is called entanglement swapping [PBWZ98]. After jointly measuring these two photons, the other two photons are in an entangled state.

This process can iteratively be extended by using multiple entangled photon pairs and corresponding measurements.

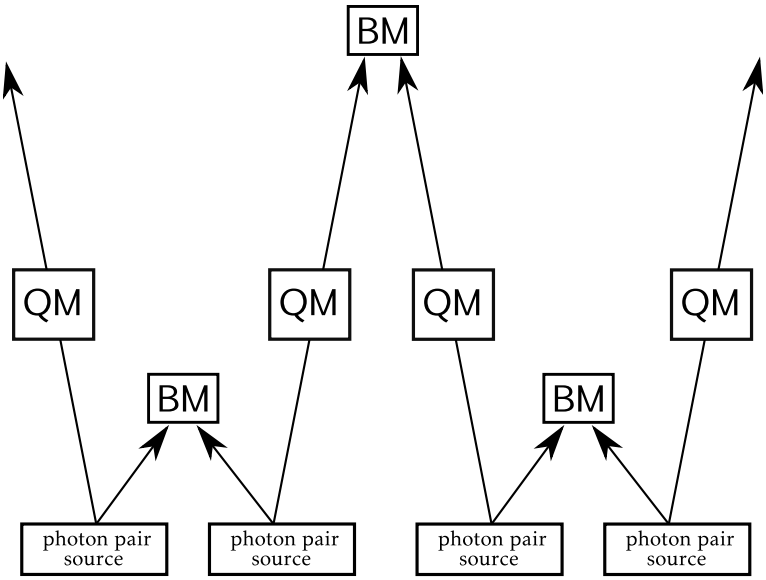

Fig. 1.1: The quantum repeater scheme (BDCZ protocol [BDCZ98]) is composed of at least two entangled photon pair sources. Two particles are sent to a Bell state measurement (BM), the other two are sent in different directions. The result of the Bell state measurement can establish the entanglement of the other two particles. The scheme is scalable to multiple sources and quantum measurements, allowing an increased distribution of entanglement. Quantum memories (QM) allow a better performance by storing the information of a flying qubit without destroying the entanglement.

For building a quantum repeater one needs sources of entangled photon pairs, modules implementing entanglement swapping and quantum memories. In Fig. 1.2 the fundamental scheme of quantum teleportation is shown. A single photon and a photon of an entangled photon pair are incident on a beam splitter. By placing detectors at two output ports of the beam splitter, the state of the incident qubit is teleported onto the flying qubit, not being measured by the two detectors.

In the frame of this work a two-color folded-sandwich down conversion source is set up, which efficiently creates polarization-entangled pairs of photons. In Sec. 2, the fundamentals of the quantum optical process of spontaneous parametric down-conversion is introduced, followed by a discussion of the principles of quantum information and of experimental tools for detecting entanglement in a generated state.
The main experimental setup, including the modified folded sandwich, the used spectrograph, the coincidence circuit and the scheme to measure the polarization correlations are shown in Sec. 3. The results of this work are shown in Sec. 4.

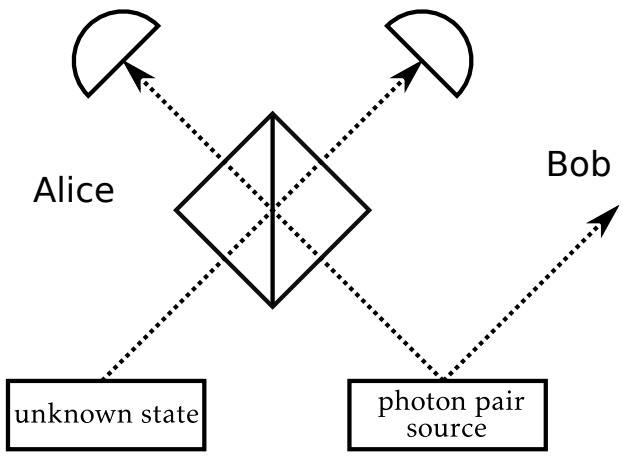

Fig. 1.2: Quantum teleportation of an unknown input state. The photon pair source is sending one photon to the Bell state measurement. By communicating the measurement result, the other photon of the pair gets entangled with the unknown input state.

2 Principles

This chapter is devoted to the theoretical foundations of this work. The nonlinear optical process known as spontaneous parametric down-conversion is discussed together with the experimental requirements for an efficient conversion of photons to photon pairs. Followed by an overview of the foundations of quantum information and quantum theory, namely entanglement, and its measurement.

2.1 Nonlinear Optics

In the field of optics one investigates light-matter interaction. Linearity is a good approximation as long as the applied electric field strength is much smaller than the field inside atoms. The polarization [Boy08] of a medium can than be written in the simple form

$$P = \epsilon_0 \chi^{(1)} E \tag{2.1}$$

where $\chi(1)$ is the linear susceptibility and ϵ_0 is the permittivity of free space. The dielectric displacement can be written as $D = \epsilon_0 E + P = \epsilon_0 \epsilon E$ whereas the refractive index of a medium is the square of the relative dielectric constant

$$n = \sqrt{\epsilon} = \sqrt{1 + \chi^{(1)}} \tag{2.2}$$

The restriction to linear interactions is not always valid. In many situations higher terms become important and one can write the polarization in terms of the electric field

$$P = \epsilon_0 \left(\chi^{(1)} E + \chi^{(2)} E^2 + \chi^{(3)} E^3 + \dots \right) \tag{2.3}$$

with the susceptibilities $\chi^{(n)}$ represented by tensors of rank $(n+1)$.

In general the second order susceptibility has 27 non-vanishing elements which may be reduced considering symmetry conditions or the exchange of the fields. The second order susceptibility is vanishing in case of crystals which obey inversion symmetry. $\chi^{(2)}$ processes are also named three-wave-mixing processes whereas $\chi^{(3)}$ processes involve four-wave-mixing [Boy08].
In this work the relevant term is of second order

$$P_i^{(2)} = \epsilon_0 \sum_{j,k} \chi_{ijk}^{(2)} E_j E_k \tag{2.4}$$

For a superposition of two monochromatic plane waves

$$E = E_1 \cos(\omega_1 t + k_1 z) + E_2 \cos(\omega_2 t + k_2 z) \tag{2.5}$$

interacting with a dielectric medium the second order polarization is

$$\begin{aligned} P^{(2)}(\omega) =& \frac{1}{2}\epsilon_0 \chi^{(2)} \Big[\underbrace{E_1^2 + E_2^2}_{\text{const}} + \underbrace{E_1^2 \cos(2\omega_1 t) + E_2^2 \cos(2\omega_2 t)}_{\text{SHG}} + \\ &+ \underbrace{2E_1 E_2 \cos(\omega_1 + \omega_2)t}_{\text{SFG}} + \underbrace{2E_1 E_2 \cos(\omega_1 - \omega_2)t}_{\text{DFG}} \Big] \end{aligned} \tag{2.6}$$

containing constant terms responsible for optical rectification where a laser beam passing through a nonlinear crystal induces an asymmetric response of material resulting in a displacement of the charges leading to a DC polarization.
The frequency dependent terms are called second harmonic generation (SHG), sum frequency generation (SFG)) and difference frequency generation (DFG). From Eq. (2.6) one can directly see that the last three terms are given rise to new frequencies.
In Fig. 2.1 the term scheme of the process of difference frequency generation is shown. This process can also be described with quantum mechanics. A pump photon with frequency ω_p decays into two lower energy photons with frequencies ω_s and ω_i. In this process the energy and momentum relations are fulfilled. Difference frequency generation

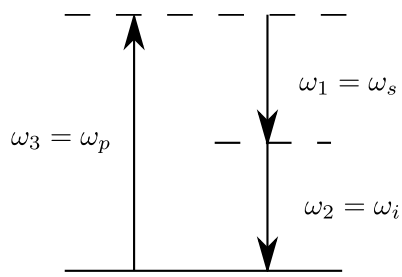

Fig. 2.1: Photon description of the interaction of three optical waves in difference-frequency generation or optical parametric amplification.

without seeding, i.e. seeded only by vacuum fluctuations, is called spontaneous parametric down conversion (SPDC) where a photon propagating in a non-centrosymmetric crystal is split spontaneously into two photons with lower frequencies. In the photon picture this process can be interpreted as the conservation of energy and momentum relations

$$\omega_p = \omega_s + \omega_i \tag{2.7}$$

$$k_p = k_s + k_i \tag{2.8}$$

This process is called a parametric process, because the process is allowed for varying pairs of frequencies obeying these conservation laws.

2.1.1 Phase Matching

The efficiency of this conversion is in general very low since the generated and fundamental waves are usually traveling at different phase velocities. This mismatch leads to energy transfer from the generated wave back to the fundamental wave after traveling the distance

$$l_c = \frac{\pi}{\Delta k} \tag{2.9}$$

which is called the coherence length. For typical nonlinear crystals this length is in the order of tens of micrometers. The phase mismatch for SHG is

$$\Delta k = k_{2\omega} - 2k_\omega = \frac{2\omega}{c}(n_{2\omega} - n_\omega) \tag{2.10}$$

or in the case of DFG

$$\Delta k = k_p - k_s - k_i \tag{2.11}$$

The highest efficiency is reached for $\Delta k = 0$. This condition can be fulfilled by fine adjustment of the crystal parameters. One technique utilizes birefringence in order to compensate for this phase mismatch, however, in order to reach some of the highest possible nonlinear coefficients, all interacting waves need to be polarized in the same direction, this situation cannot be reached using birefringence. Another technique allowing all three waves to be polarized along the same direction was first proposed by Armstrong et al. in 1962 [ABDP62]. This technique is called quasi phase-matching, it compensates the mismatch by using an optical material with a certain periodic structure, an example is depicted in Fig. 2.2.

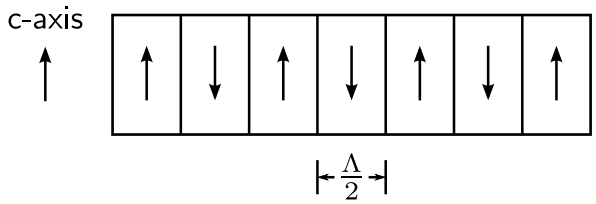

Fig. 2.2: Second-order nonlinear optical crystal, with changing orientation of the the c-axis with period Λ. This setup is also called periodically poled material.

For example, by reversing the orientation of the c-axis with period Λ along the direction of propagation, the result for the phase mismatch is in first order

$$\Delta k_{QPM} = k_p - k_s - k_i - \frac{2\pi}{\Lambda} \tag{2.12}$$

and for the nonlinear coupling coefficient [Boy08] one has

$$d_{QPM} = \frac{2}{\pi} d_{eff} \tag{2.13}$$

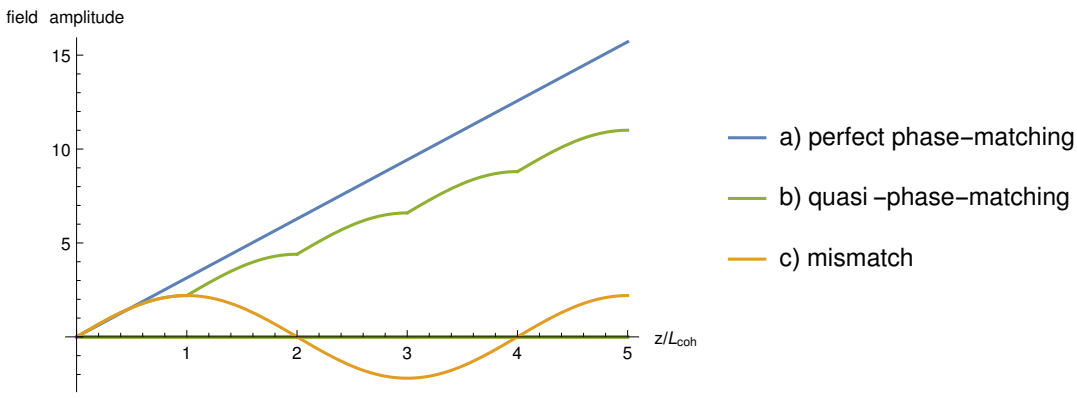

Fig. 2.3: Comparison of the spatial variation of the field amplitude of the generated wave. Curve (a) represents perfect phase-matching, curve (c) assumes a nonzero wavevector mismatch Δk and curve (b) assumes a quasi-phase-matched interaction.

This technique can be implemented by applying the field of an electrode pattern to a ferroelectric material. This will lead to an inversed crystalline c axis for the material lying directly under the electrodes. The consequences of different phase-matching conditions on the generated field amplitude is shown in Fig. 2.3.

2.1.2 Nonlinear Optics with Focused Gaussian Beams

In order to reach high conversion efficiencies the pump wave is usually focused inside the nonlinear crystal. The field of an electromagnetic wave in paraxial approximation is given by

$$E(\vec{r}) = E_0 \frac{w_0}{w(z)} \exp\left(-\frac{x^2+y^2}{w^2(z)}\right) \exp\left(ikz + ik\frac{x^2+y^2}{2R(z)} + i\xi(z)\right) \tag{2.14}$$

with a Gaussian intensity profile called a Gaussian light beam. Its parameters are the beam radius

$$w = w_0\sqrt{1+(z/z_0)^2} \tag{2.15}$$

with Rayleigh range z_0 and beam waist $w_0 = \sqrt{\lambda z_0/\pi}$, radius of curvature of the wavefronts $R(z) = z\left[1+(z_0/z)^2\right]$ and the phase retardation $\xi(z) = \arctan(z/z_0)$. The optical intensity $I(\vec{r}) = |E(\vec{r})|^2$ is a function of the axial and radial position.
Boyd and Kleinman [BK68, Boy08] calculate an optimal focus parameter considering high efficiency for the parametric interaction of focused Gaussian laser beams. They find that the highest efficiency is obtained when beam walk-off effects are negligible, when the focus of the incident laser beam is located at the center of the crystal, the ratio between the crystal length L and the confocal parameter $b = kw^2$ is

$$L/b = 2.84 \tag{2.16}$$

and when the wavevector mismatch is set equal to

$$\Delta k = 3.2/L \tag{2.17}$$

Another, more recent analysis by Bennink [Ben10], for collinear Gaussian beams, finds the same optimal parameters. However, assuming a fixed pump parameter

$$\xi_p = L/(k_p w_p^2) \tag{2.18}$$

he finds that the optimal parameters are

$$\xi_s = \xi_i = \sqrt{2.84\xi_p} \tag{2.19}$$

2.1.3 Spontaneous Parametric Down-Conversion

In the experiment, a periodically poled, nonlinear crystal is converting pump photons into pairs of lower energy photons. This nonlinear optical process is known as DFG without seeding with an idler or a signal field. Since the photons are spontaneously decaying into lower and one can parametrically adjust the phase matching conditions this process is commonly named spontaneous parametric down-conversion. Other names for SPDC are parametric fluorescence or parametric scattering. This process allows the relatively easy production of highly correlated photon pairs [Ou07]. It cannot be described by classical nonlinear wave-equations, however, in a semi-classical picture, it can be interpreted as an optical parametric oscillator seeded by the spontaneous fluctuations of the vacuum field. Spontaneous parametric down-conversion can formally be described by the interaction Hamiltonian

$$\hat{H}_I \propto \hat{a}_p \hat{a}_1^\dagger \hat{a}_2^\dagger + h.c. \tag{2.20}$$

where $\hat{a}_i^\dagger$ and $\hat{a}_i$ are the respective creation and annihilation operators for the three modes. In the next step the pump field is normally treated as classical and non depleted. In the limit of weak interaction strength, i.e. small non-linearities, one derives the resulting state of the down-conversion process

$$|\Psi_{SPDC}\rangle = |0\rangle_1 |0\rangle_2 + \gamma |1\rangle_1 |1\rangle_2 + \gamma^2 |2\rangle_1 |2\rangle_2 + \dots \tag{2.21}$$

In general, modes 1 and 2 can be treated non-degenerate, fulfilling energy conservation

$$\omega_p = \omega_1 + \omega_2 \tag{2.22}$$

For weak interaction strength and pump fields, i.e. $\gamma \ll 1$, all higher order terms may be neglected. Under these circumstances the detection of a photon in mode 1 heralds a single photon Fock state in mode 2, and vice versa. This can be seen by projection on a single photon state

$$\langle 1|_1 |\Psi_{SPDC}\rangle = \langle 1|_1 (|0\rangle_1 |0\rangle_2 + \gamma |1\rangle_1 |1\rangle_2) = \gamma |1\rangle_2 \tag{2.23}$$

A disadvantage of this kind of source is that the pair production is a probabilistic process and that by scaling to higher pump powers, higher order terms can become non-negligible, creating significant unwanted error terms.

The full quantum treatment with a single photon input state is an interesting case. The Hamiltonian and its corresponding time evolution operator can be written as

$$\hat{H}_I = \gamma(\hat{a}_p \hat{a}_1^\dagger \hat{a}_2^\dagger + h.c.) \tag{2.24}$$

$$\hat{U}(t) = e^{-i\hat{H}_I t/\hbar} = e^{i\gamma t/\hbar(\hat{a}_p \hat{a}_1^\dagger \hat{a}_2^\dagger + h.c.)} \tag{2.25}$$

Without loss, under this evolution the states $|100\rangle$ and $|011\rangle$ form a closed system, since no other states outside the Hilbert space spanned by those two states can be created from them. By assuming initially empty signal and idler modes and the pump field being in a single photon Fock state

$$|\Psi(0)\rangle = |100\rangle \tag{2.26}$$

and by introducing the abbreviation $\hat{a}_{DC} = \hat{a}_p \hat{a}_1^\dagger \hat{a}_2^\dagger$ and $\gamma/\hbar = \Omega$ the state evolution is

$$|\Psi(t)\rangle = \hat{U}(t)\,|\Psi(0)\rangle \tag{2.27}$$

$$= e^{-i\Omega t(\hat{a}_{DC}^\dagger + h.c.)}\,|100\rangle \tag{2.28}$$

by expanding the exponential into a series one yields

$$|\Psi(t)\rangle = \cos(\Omega t)\,|100\rangle - i\sin(\Omega t)\,|011\rangle \tag{2.29}$$

Mathematically, this derivation is analogous to a two level atomic system driven by a resonant, coherent laser field giving rise to Rabi oscillations, i.e. the probabilities for the two states are periodically oscillating. In principle, this process can be 100 % efficient, however, Ωt is determined by the pump field, the effective non-linear coefficient and the finite crystal length.

2.2 Quantum Information

In this section the fundamental formalism of quantum information is discussed. The description of a qubit is formulated as well as operations on qubits in the form of quantum mechanical operators.

2.2.1 Qubits

A qubit is a quantum mechanical state vector that describes a physical system with two distinct physical states $|0\rangle$ and $|1\rangle$ [NC10]. The two states are orthogonal and the superposition is also an allowed state of the system

$$|\psi\rangle = a_1\,|0\rangle + a_2\,|1\rangle \tag{2.30}$$

where a_1 and a_2 are complex numbers. The normalization condition $\langle\psi|\psi\rangle = 1$ is equivalent to

$$|a_1|^2 + |a_2|^2 = 1 \tag{2.31}$$

Experimental realizations for a qubit are for example two orthogonal polarization states of a photon, the two orientations of a spin half particle, a pair of electronic energy levels in an atom or a quantum dot or a pair of paths in an interferometer. For example a single photon described in the basis defined by the two orthogonal state vectors $|0\rangle = |H\rangle$ and $|1\rangle = |V\rangle$ representing orthogonal horizontal and vertical polarization states. Qubits can be treated with the help of the following Pauli operators and the identity operator

$$\hat{I} = |H\rangle\langle H| + |V\rangle\langle V| \tag{2.32}$$

$$\hat{\sigma}_x = |H\rangle\langle V| + |V\rangle\langle H| \tag{2.33}$$

$$\hat{\sigma}_y = i\left(|V\rangle\langle H| + |H\rangle\langle V|\right) \tag{2.34}$$

$$\hat{\sigma}_z = |H\rangle\langle H| - |V\rangle\langle V| \tag{2.35}$$

This basis is commonly called standard computational basis $\{|H\rangle, |V\rangle\}$. The state vector of the single photon can also be written as a vector

$$\Psi = c_0|H\rangle + c_1|V\rangle = \begin{pmatrix} c_0 \\ c_1 \end{pmatrix} \tag{2.36}$$

and the operators above can be expressed as the following matrices

$$I = \begin{pmatrix} 1 & 0 \\ 0 & 1 \end{pmatrix}, \quad \sigma_x = \begin{pmatrix} 0 & 1 \\ 1 & 0 \end{pmatrix}, \quad \sigma_y = \begin{pmatrix} 0 & -i \\ i & 0 \end{pmatrix}, \quad \sigma_z = \begin{pmatrix} 1 & 0 \\ 0 & -1 \end{pmatrix} \tag{2.37}$$

For example the operator σ_z has eigenvalues $+1$ and -1 with corresponding eigenvectors $|H\rangle$ and $|V\rangle$.

Qubit states can be represented by points on the surface of the Bloch sphere where each point on the surface corresponds to a differently prepared state. The Bloch sphere is given by the eigenvectors of the Pauli matrices. A general qubit state on the Bloch sphere can be written as

$$|\psi_{\theta,\phi}\rangle = \cos\left(\frac{\theta}{2}\right)|H\rangle + e^{i\varphi}\sin\left(\frac{\theta}{2}\right)|V\rangle \tag{2.38}$$

A general observable $\hat{\sigma}_{\theta,\phi}$ is given in terms of the Pauli operators

$$\hat{\sigma}_{\theta,\phi} = \cos\phi\sin\theta\hat{\sigma}_x + \sin\phi\sin\theta\hat{\sigma}_y + \cos\theta\hat{\sigma}_z \tag{2.39}$$

For example $\sigma_{0,0} = \sigma_z$, $\sigma_{\frac{\pi}{2},0} = \sigma_x$ or $\sigma_{\frac{\pi}{2},\frac{\pi}{2}} = \sigma_z$. The probability to measure a horizontal polarization, for example, when having the general qubit state (2.38) is given by the expectation value of the projection operator $\hat{P}_H = 1/2(\hat{I} + \hat{\sigma}_z)$:

$$\langle\psi_{\theta,\phi}|\hat{P}_H|\psi_{\theta,\phi}\rangle = \langle\psi_{\theta,\phi}|\frac{1}{2}(\hat{I} + \hat{\sigma}_z)|\psi_{\theta,\phi}\rangle \tag{2.40}$$

$$= \cos^2\frac{\theta}{2} \tag{2.41}$$

This is an example for a single qubit measurement. In the next section the properties of two-qubit systems will be discussed, in these system one can observe entanglement.

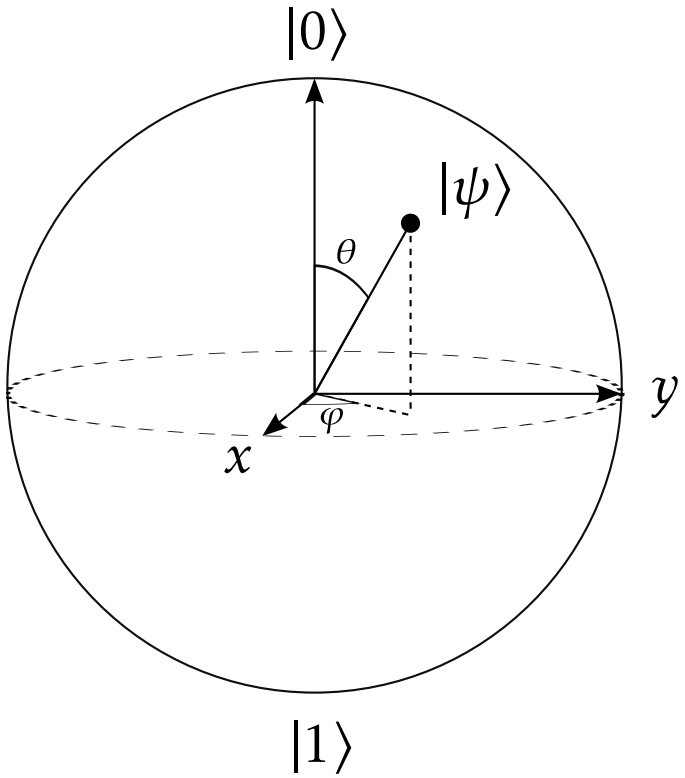

Fig. 2.4: A general qubit state of the form (2.38) can be represented on the Bloch sphere. The two orthogonal states $|0\rangle$ and $|1\rangle$, i.e. horizontally and vertically polarized light, are represented by two points lying on opposite sides of the sphere.

2.2.2 Entangled states

Entanglement is a central element in quantum information. It is a property of multipartite quantum systems consisting of two or more quantum systems. A two-qubit state can be written as a tensor product of the two single-qubit states, the direct product

$$|H\rangle \otimes |H\rangle = |H\rangle\,|H\rangle = |HH\rangle \tag{2.42}$$

In the standard computer basis the corresponding state vector can be written as

$$|HH\rangle \rightarrow \begin{pmatrix} 1 \\ 0 \\ 0 \\ 0 \end{pmatrix} \tag{2.43}$$

A more general two-qubit state can be written using the fundamental superposition principle of quantum mechanics, for example the superposition of two product states

$$|\Psi\rangle = \frac{1}{\sqrt{2}}\left(|H\rangle\,|H\rangle + |V\rangle\,|V\rangle\right) \tag{2.44}$$

is also an allowed state of the system. This state cannot be written as a product of a state for System 1 and one for System 2, i.e. it is not factorizable, and is called an entangled state. There exist four maximally entangled two-qubit states that are a basis of the four dimensional Hilbert space, the Bell-states

$$|\psi^-\rangle = \frac{1}{\sqrt{2}}\Big(|H\rangle\,|V\rangle - |V\rangle\,|H\rangle\Big) \tag{2.45}$$

$$|\psi^+\rangle = \frac{1}{\sqrt{2}}\Big(|H\rangle\,|V\rangle + |V\rangle\,|H\rangle\Big) \tag{2.46}$$

$$|\phi^-\rangle = \frac{1}{\sqrt{2}}\Big(|H\rangle\,|H\rangle - |V\rangle\,|V\rangle\Big) \tag{2.47}$$

$$|\phi^+\rangle = \frac{1}{\sqrt{2}}\Big(|H\rangle\,|H\rangle + |V\rangle\,|V\rangle\Big) \tag{2.48}$$

the state $|\psi^-\rangle$ is antisymmetric under the exchange of the two qubits and has zero total angular momentum. The other three states are symmetric under permutation and span the space with unit angular momentum. Each Bell state can be converted to any other Bell state by a unitary transformation carried out on one of the two qubits

$$|\phi^+\rangle = (\hat{I} \otimes \hat{\sigma}_z)\,|\phi^-\rangle = (\hat{I} \otimes \hat{\sigma}_x)\,|\psi^+\rangle = (\hat{I} \otimes \hat{\sigma}_y)\,|\psi^-\rangle \tag{2.49}$$

The transformation of one qubit changes the complete state, this property gives rise to non-local behavior discussed by Einstein, Podolski and Rosen (EPR) in their famous paper "Can quantum mechanical description of physical reality be considered complete?" [EPR35], since for a local realistic theory the measurement of one particle, spatially separated from the other, should not influence the second one.

In contrast to separable states, that are correlated only along one two-photon basis, entangled states are correlated in more than one basis. This makes it impossible to determine the single photon state.

In the case of quantum systems containing three single qubits it is also possible to find maximally entangled states, for example the famous Greenberger-Horne-Zeilinger state $|GHZ\rangle$ or the Werner state $|W\rangle$

$$|GHZ\rangle = \frac{1}{\sqrt{2}}(|000\rangle + |111\rangle), \quad |W\rangle = \alpha\,|001\rangle + \beta\,|010\rangle + \gamma\,|001\rangle \tag{2.50}$$

2.2.3 Einstein, Podolsky and Rosen

"Can quantum mechanical description of physical reality be considered complete?"

Under the assumption that quantum mechanical description is complete, EPR show that this leads to a contradiction. They consider two systems that interact for a period of time δt and then getting separated. The total state of system may be

$$\psi(x_1, x_2) = \sum_{n=1}^{\infty} \psi_n(x_2) u_n(x_1) = \sum_{i=1}^{\infty} \xi_i(x_2) v_i(x_1) \tag{2.51}$$

with the eigenfunctions $u_n(x_1)$ and eigenvalues a_n of operator $\hat{A}$ of the first system and corresponding coefficients $\psi_n(x_2)$, x_2 denoting the second system. $v_n(x_1)$ are the eigenfunctions of operator $\hat{B}$ with coefficients $\xi_n(x_2)$. By measuring the observable A with result a_k, the physical state of the system after measurement by projection of $\psi(x_1, x_2)$ on the corresponding eigenvector $u_k(x_1)$ is

$$\psi(x_1, x_2) = \psi_k(x_2) u_k(x_2) \tag{2.52}$$

By measuring observable B with possible eigenvalues b_i, the state of the system after the measurement is given by

$$\psi(x_1, x_2) = \xi_r(x_2) v_r(x_1) \tag{2.53}$$

in case the measurement result is b_r. That is, according to which measurement has taken place on System 1, a different state describes System 2.

EPR conclude that since both systems are separated after measurement and should not interact anymore, a measurement on one system should not change the state of the other system and therefore the two different wave functions cannot describe the same physical reality.

Going further, EPR consider the case that the eigenfunctions $\psi_k(x_2)$ and $\xi_r(x_1)$ that describe the system belong to two non-commuting operators $\hat{P}$ and $\hat{Q}$ with corresponding eigenvalues p_k and q_r. It would then be possible, by measuring $\hat{A}$ or $\hat{B}$, to find the value of $\hat{P}$ or $\hat{Q}$ without disturbing the second system. The definition of reality enforces, that $\hat{P}$ and $\hat{Q}$ need to be an element of physical reality. Since it has been shown that both

wave functions belong to the same physical reality, the two observables P and Q must simultaneously be an element of physical reality.

This leads to a contradiction, since two non-commuting observables cannot be precise measured simultaneously, therefore they cannot be an element of physical reality. EPR conclude that the quantum mechanical description of reality using the wave functions cannot be complete.

This opens the question whether hidden variables have to be introduced, specifying the properties of the system, or if local realism has to be abandoned in order to complete quantum mechanics. The operators values would then be always defined and specify the measurement results.

Bohm and Aharonov

In their thought experiment [BA57] considering a special case of the above EPR experiments using a molecule with zero total spin, consisting of two atoms with spin-$\frac{1}{2}$. The wave function is then given by

$$\psi = \frac{1}{\sqrt{2}}\Big[\psi_+(1)\psi_-(2) - \psi_-(1)\psi_+(2)\Big] \tag{2.54}$$

with the wave-function $\psi_\pm(i)$ describing the state in which spin of particle i has the value $\pm\frac{\hbar}{2}$ with respect to an arbitrary quantization axis.

Now the atoms are getting separated, permitting any interaction. By measuring of one spin component of the first particle, one directly gets the spin component of the other particle. The direction of spin measurement can be chosen freely. After the measurement only this one chosen component has a definite value, the other spin components are uncertain.

This thought experiment is therefore asking the question, why does particle 2 "'know"' about which component was measured at particle 1, although any interaction between the two particles was permitted.

Bohm proposed a practical test of the described experiment using photons. For photons the respective wave function has the following form

$$\psi = \frac{1}{\sqrt{2}}\Big[\psi_x(1)\psi_y(2) - \psi_y(1)\psi_x(2)\Big] \tag{2.55}$$

where $\psi_{x,y}(i)$ describe arbitrarily chosen orthogonal polarization states. State (2.55) is rotationally invariant and has the same properties with respect to correlations as state (2.54). For photons however, since they are spin-1 particles all angles of measurement apparatuses are only half the value compared with spin-$\frac{1}{2}$ particles. The following abbreviations of Bell inequalities rely on this thought experiment assuming spin-$\frac{1}{2}$ particles.

2.2.4 Bell Inequalities

In the following, a few Bell inequalities are discussed. A violation of these inequalities rules out the existance of local hidden-variable theories. A violation of these inequalities is only possible for entangled states.

Bell's original inequality

In his 1964 paper [Bel64], Bell shows that the assumption of local hidden variables leads to contradiction with the statistical predictions of quantum mechanics by considering a pair of spin-$\frac{1}{2}$ particles flying in opposite directions. The wave function describing this system is

$$|\psi\rangle = \frac{1}{\sqrt{2}} \left(|\uparrow\rangle_1 |\downarrow\rangle_2 - |\downarrow\rangle_1 |\uparrow\rangle_2 \right) \tag{2.56}$$

One can now measure the spin of each particle along arbitrary directions $\vec{a}$, $\vec{b}$, with the assumption $|\vec{a}| = |\vec{b}| = 1$. This measurement corresponds to the quantum mechanical operators $\vec{\sigma}_1 \cdot \vec{a}$ and $\vec{\sigma}_2 \cdot \vec{b}$ where $\vec{\sigma}$ is the spin operator consisting of the Pauli matrices $\vec{\sigma} = \{\hat{\sigma}_x, \hat{\sigma}_y, \hat{\sigma}_z\}$. Measuring the spin of each particle along the same axis $\vec{a}$, the results are always anti-correlated.
Bell then introduces a an additional set of variables λ, assuming a normed probability distribution

$$\int \mathrm{d}\lambda \, \rho(\lambda) = 1 \tag{2.57}$$

Let $A(\vec{a}, \lambda)$ be the measurement result of $\vec{\sigma}_1 \cdot \vec{a}$ and $B(\vec{b}, \lambda)$ the measurement result of $\vec{\sigma}_2 \cdot \vec{b}$. Thus the results of a measurement on one particle depend on the supplementary variables, and not on the measurement direction of the second particle. The measurement results can have the following values

$$A(\vec{a}, \lambda) = \pm 1 \tag{2.58}$$

$$B(\vec{b}, \lambda) = \pm 1 \tag{2.59}$$

The expectation value for measuring the product $A(\vec{a}, \lambda) B(\vec{b}, \lambda)$ is given by

$$P(\vec{a}, \vec{b}) = \int \mathrm{d}\lambda \, \rho(\lambda) A(\vec{a}, \lambda) B(\vec{b}, \lambda) \tag{2.60}$$

This should be equal to the quantum mechanical prediction, in this case, the expectation value for the singlet state

$$\langle \psi | \vec{\sigma}_1 \cdot \vec{a} \;\; \vec{\sigma}_2 \cdot \vec{b} | \psi \rangle = -\vec{a} \cdot \vec{b} \tag{2.61}$$

For comparison, the correlation function for an isotropic mixture of product states is

$$-\frac{1}{3} \vec{a} \cdot \vec{b} \tag{2.62}$$

If $P(\vec{a}, \vec{b})$ is equal the quantum mechanical value, the following conditions have to be fulfilled

$$P(\vec{a}, \vec{b}) = -P(\vec{a}, \vec{b}) = -1, \text{ if } \vec{a} || \vec{b} \tag{2.63}$$

$$P(\vec{a}, \vec{b}) = 0, \text{ if } \vec{a} \perp \vec{b} \tag{2.64}$$

$P(\vec{a},\vec{b})$ can only be -1, if $\vec{a}=\vec{b}$ and $A(\vec{a},\lambda)=-B(\vec{b},\lambda)$

$$P(\vec{a},\vec{b}) = -\int \mathrm{d}\lambda\rho(\lambda)A(\vec{a},\lambda)A(\vec{b},\lambda) \tag{2.65}$$

Suppose $\vec{c}$ is another unit vector

$$P(\vec{a},\vec{b}) - P(\vec{a},\vec{c}) = -\int \mathrm{d}\lambda\rho(\lambda)\left[A(\vec{a},\lambda)A(\vec{b},\lambda) - A(\vec{a},\lambda)A(\vec{c},\lambda)\right] \tag{2.66}$$

$$= \int \mathrm{d}\lambda\rho(\lambda)A(\vec{a},\lambda)A(\vec{b},\lambda)\left[A(\vec{b},\lambda)A(\vec{c},\lambda) - 1\right] \tag{2.67}$$

assuming that $A(\vec{b},\lambda)^2 = 1$. By squaring both sides and using the Cauchy-Schwarz inequality yields

$$\left|P(\vec{a},\vec{b}) - P(\vec{a},\vec{c})\right| = \left|\int \mathrm{d}\lambda\rho(\lambda)A(\vec{a},\lambda)A(\vec{b},\lambda)\left[A(\vec{b},\lambda)A(\vec{c},\lambda) - 1\right]\right| \tag{2.68}$$

$$\leq \int \mathrm{d}\lambda\rho(\lambda)\left|\left[A(\vec{b},\lambda)A(\vec{c},\lambda) - 1\right]\right| \tag{2.69}$$

$$= \int \mathrm{d}\lambda\rho(\lambda)\left[1 - A(\vec{b},\lambda)A(\vec{c},\lambda)\right] \tag{2.70}$$

$$= 1 + P(\vec{b},\vec{c}) \tag{2.71}$$

One gets an inequality that must hold for theories with local hidden variables, the Bell inequality

$$\left|P(\vec{a},\vec{b}) - P(\vec{a},\vec{c})\right| \leq 1 + P(\vec{b},\vec{c}) \tag{2.72}$$

For some values $\vec{a},\vec{b}$ this inequality is violated by the predictions of quantum mechanics. For example, by choosing $\vec{a}\cdot\vec{c}=0$ and $\vec{a}\cdot\vec{b}=\vec{b}\cdot\vec{c}=\frac{1}{\sqrt{2}}$, it follows

$$\left|P(\vec{a},\vec{b}) - P(\vec{a},\vec{c})\right| - P(\vec{b},\vec{c}) = \left|-\vec{a}\vec{b} + \vec{a}\vec{c}\right| + \vec{a}\vec{b} = \sqrt{2} \geq 1 \tag{2.73}$$

Clauser, Horne, Shimony and Holt's inequality (CHSH)

The inequality by CHSH [CHSH69] is a modified Bell inequality formulated with respect to imperfect correlations and measurement apparatuses.

$$\left|P(\vec{a},\vec{b}) - P(\vec{a},\vec{c})\right| + P(\vec{b}',\vec{c}) + P(\vec{b}',\vec{b}) \leq 2 \tag{2.74}$$

The upper bound for local realistic theories is 2. The quantum mechanical prediction for this inequality is $2\sqrt{2}$.

2.2.5 Entanglement measures

In the last sections different formulations of Bell's inequality were introduced. A violation of Bell's inequality shows the non-locality of quantum mechanics and directly shows that the generated state is entangled. However, not all entangled states do violate such an inequality. The detection of multi-partite entanglement can be implemented in various other ways.

Visibility

As a starting point for the detection of entanglement, one can measure series of correlations, or joint-measurement probabilities. One can then identify correlations that are uniquely connected to entangled quantum systems. One measure leading to entanglement is a visibility of $V = 1$ [WGP+07]. The visibility is defined as

$$V_{H/V} = \frac{P_{HH} - P_{HV}}{P_{HH} + P_{HV}} \tag{2.75}$$

where P_{ij} is the joint-measurement probability

$$P_{ij} = Tr\left[\hat{\rho}\left|ij\right\rangle\left\langle ij\right|\right] = \left|\left\langle ij|\psi\right\rangle\right|^2 \tag{2.76}$$

of seeing the state $|ij\rangle$. The visibility can be measued by calculating only 2 joint-measurement probabilities. A visibility of 100% is leading to entanglement, but it is not already sufficient to say that the generated state is an entangled state, since separable states can also show this behavior. However, an ideal Bell-state is showing 100% visibility in all measurement bases, this behavior cannot be reproduced with separable states.
In experimental situations, generating non-maximally entangled states, one needs tools that are able to discriminate between separable and non-maximally entangled states with a minimum amount of effort. In the following two sections two unambiguous entanglement indicators are discussed, the Bell-state fidelity F and the entanglement witness W.

Bell-state fidelity

Another way to detect entanglement in a generated state is the Bell-state fidelity F [Uhl76], which is the measure of the overlap between the two states $\hat{\rho}_1$ and $\hat{\rho}_2$

$$F(\hat{\rho}_1, \hat{\rho}_2) = \left(Tr\left[\sqrt{\sqrt{\hat{\rho}_2}\hat{\rho}_1\sqrt{\hat{\rho}_2}}\right]\right)^2 \tag{2.77}$$

The Bell-state fidelity quantifies how well an experimental state $\hat{\rho}_1$ resembles another general state $\hat{\rho}_2$ [WGP+07]. In the case of a pure reference state the fidelity simplifies to

$$F(\hat{\rho}_1, \hat{\rho}_2) = Tr\left[\hat{\rho}_2\hat{\rho}_1\right] \tag{2.78}$$

For an ideal Bell-state of the form $|\phi^+\rangle = \frac{1}{\sqrt{2}}\left(|HH\rangle + |VV\rangle\right)$ the fidelity with the measured state $\hat{\rho}$ is

$$F_{\phi^+} = \langle\phi^+|\hat{\rho}|\phi^+\rangle = Tr\left[\hat{\rho}\left|\phi^+\right\rangle\left\langle\phi^+\right|\right] \tag{2.79}$$

If $F_{\phi^+} > \frac{1}{2}$, the state is entangled, while for any separable state the fidelity is $F_{\phi^+} \leq \frac{1}{2}$. The full two-qubit density matrix $\hat{\rho}$ can be measured by a photonic state tomography [AJK, JKMW01], which requires 16 joint-measurement probabilities. This is not

necessary, since for determining the Bell-state fidelity one only needs to calculate 6 joint-measurement probabilities,

$$F_{\phi^+} = \frac{1}{2}\left(P_{HH} + P_{VV} + P_{DD} + P_{AA} - P_{RR} - P_{LL}\right) \tag{2.80}$$

$$F_{\phi^-} = \frac{1}{2}\left(P_{HH} + P_{VV} - P_{DD} - P_{AA} + P_{RR} + P_{LL}\right) \tag{2.81}$$

where P_{ij} are the joint-measurement probabilities and the indices i and j indicate the basis of measurement. In the standard computer basis of optical polarization with horizontal $|H\rangle \equiv |0\rangle$ and vertical $|V\rangle \equiv |1\rangle$ direction of polarization, the equal-weight real superpositions are diagonal $|D\rangle$ and anti-diagonal $|A\rangle$ polarizations

$$|D\rangle = \frac{1}{\sqrt{2}}\left(|H\rangle + |V\rangle\right) \tag{2.82}$$

$$|A\rangle = \frac{1}{\sqrt{2}}\left(|H\rangle - |V\rangle\right) \tag{2.83}$$

and the complex equal-weight superpositions are

$$|R\rangle = \frac{1}{\sqrt{2}}\left(|H\rangle + i\,|V\rangle\right) \tag{2.84}$$

$$|L\rangle = \frac{1}{\sqrt{2}}\left(|H\rangle - i\,|V\rangle\right) \tag{2.85}$$

Another way to witness the fidelity is the following equation [GT09, SRJ+13]

$$F = \langle\phi^\pm|\rho|\phi^\pm\rangle \tag{2.86}$$

$$= \left(1 + V_{H/V} \pm V_{D/A} \mp V_{L/R}\right)/4 \tag{2.87}$$

where $V_{ij} = (N_{ii} + N_{jj} - Nij - N_{ji})/(N_{ii} + N_{jj} + Nij + N_{ji})$ are the visibilites in 3 mutually unbiased measurement bases and N_{ij} are the detected coincidence counts.

Entanglement witness

Another tool for detecting entanglement is the entanglement witness W [Ter02,LKCH00]. It is an approach to distinguish separable states from entangled states. An entanglement witness is an observable W, this observable is constructed to show a negative expectation value on any entangled state $\hat{\rho}$ and stays strictly positive for any separable state $\hat{\rho}$. Therefore W witnesses the entanglement of a generated state $\hat{\rho}$. Furthermore, it has been shown [HHH96, Wor76] that one can find a suitable entanglement witness $\hat{W}$ for every entangled state.

An entanglement witness for a state $\hat{\rho}$ can be constructed by taking an Hermitian operator $\hat{W}$ satisfying the two conditions

$$Tr\left[\hat{\rho}_{entangled}\hat{W}\right] < 0 \tag{2.88}$$

$$Tr\left[\hat{\rho}_{separable}\hat{W}\right] \geq 0 \tag{2.89}$$

The entanglement witness $\hat{W}$ discriminates between separable and entangled quantum states by analyzing the geometry of the state space.

An optimal witness operator W is given by

$$\hat{W} = (|e_{min}\rangle \langle e_{min}|)^{T_a} \tag{2.90}$$

where $|e_{min}\rangle$ is the eigenvector of $\hat{\rho}^{T_a}$ corresponding to the eigenvalue $\lambda_{min} < 0$ and T_a is the partial transpose on the a-th qubit. For the four Bell states one then finds the following witness operators [GT09]

$$\hat{W}(\phi^+) = \frac{1}{2}(-|HH\rangle\langle VV| - |VV\rangle\langle HH| + |HV\rangle\langle HV| + |VH\rangle\langle VH|) \tag{2.91}$$

$$\hat{W}(\phi^-) = \frac{1}{2}(+|HH\rangle\langle VV| + |VV\rangle\langle HH| + |HV\rangle\langle HV| + |VH\rangle\langle VH|) \tag{2.92}$$

$$\hat{W}(\psi^+) = \frac{1}{2}(+|HH\rangle\langle HH| + |VV\rangle\langle VV| - |HV\rangle\langle VH| - |VH\rangle\langle HV|) \tag{2.93}$$

$$\hat{W}(\psi^-) = \frac{1}{2}(+|HH\rangle\langle HH| + |VV\rangle\langle VV| + |HV\rangle\langle VH| + |VH\rangle\langle HV|) \tag{2.94}$$

Like for the Bell state fidelity it is also not necessary to measure the full density matrix. For the ideal Bell state $|\phi^+\rangle$ the decomposition is

$$\langle \hat{W}_{\phi^+} \rangle = \frac{1}{2}(P_{HV} + P_{VH} - P_{DD} - P_{AA} + P_{RR} + P_{LL}) \tag{2.95}$$

$$\langle \hat{W}_{\phi^-} \rangle = \frac{1}{2}(P_{HV} + P_{VH} + P_{DD} + P_{AA} - P_{RR} - P_{LL}) \tag{2.96}$$

The witness can also be written as

$$\hat{W}_{\phi^+} = \left(|\psi^+\rangle\langle\psi^+|\right)^{T_2} = \frac{1}{2} I \otimes I - |\phi^+\rangle\langle\phi^+| \tag{2.97}$$

where T_2 is the partial transpose operation on the second qubit. The condition for the detection of an entangled state is $\langle \hat{W}_{\phi^+} \rangle = Tr\,(W_{\phi^+}\hat{\rho}) < 0$, then

$$Tr\left[\hat{W}_{\phi^+}\hat{\rho}\right] = \frac{1}{2} - Tr\left[\hat{\rho}\,|\psi^+, \phi^+\rangle\langle\psi^+, \phi^+|\right] \tag{2.98}$$

$$= \frac{1}{2} - F_{\psi^+,\phi^+} \tag{2.99}$$

One can see that if $\langle \hat{W}_{\psi^+,\phi^+} \rangle < 0$, then this is equivalent to $F_{\psi^+,\phi^+} > \frac{1}{2}$, which is simply the Bell-state fidelity indicator [WGP+07].
To address for an experimental situation one can introduce noise, represented by a mixed state $\hat{\chi}$. The generated state can then be written as

$$\hat{\rho} = p\,|\phi^+\rangle\langle\phi^+| + (1-p)\hat{\chi} \tag{2.100}$$

where p is the probability of having produced the ideal Bell state $|\phi^+\rangle$. These kinds of states are called Werner states [BDMDN$^+$03, Per96].

Summarizing, in order to detect an entangled state, one can measure the visibility $V_{H/V}$ in the standard computational basis. A visibility of $V_{H/V} = 1$ is leading to entanglement, however, this behavior can also be measured for a separable state. Unambiguous entanglement indicators are the Bell-state fidelity of $F > \frac{1}{2}$ or an entanglement witness of $W < 0$. Both measures can be calculated out of 6 joint-probability measurements. Alternatively, one can perform a complete two-qubit quantum state tomography involving 16 joint-probability measurements and reconstruct the two-qubit density matrix $\hat{\rho}$ of the generated state.

3 Experimental Setup

This section explains in detail the generation of polarization-entangled photon pairs in the folded sandwich scheme. The fundamental experimental setup is shown as well as the experimental scheme to analyze the spectral properties of the emission and additionally the properties of an optimal single-mode coupling is discussed. Finally, the setup for assessing the polarization correlations is shown.

3.1 Two-color Folded Sandwich

3.1.1 Linear double pass scheme

The folded sandwich scheme [SRJ+13], depicted in Fig. 3.1, consists of various optical elements. As a pump source, light from a 532 nm continuous wave laser gets linearly polarized before rotated to a superposition of horizontal and vertical polarization using a $\frac{\lambda}{2}$-wave-plate. Any circular components can be deleted by a $\frac{\lambda}{4}$-wave-plate and thus enables us to finely reach a high conversion efficiency.

A plano-covex lens f_p is focusing the continuous wave pump light inside the periodically poled nonlinear crystal (MgO:PPLN). Inside the crystal, the pump photons are spontaneously split into a photon pair under conservation of energy and momentum. This process is happening with small probability in the order of $10^{-7}\,\mathrm{s}^{-1}$ per pump photon (see Sec. 4.2.3). The probability of this conversion is maximized by optimized focusing of the pump photons using the lens f_p. Due to phase-matching of type-0, the generated pair of photons is vertically polarized. Its polarization gets transformed into horizontal direction by a double pass through a Fresnel rhomb. This is discussed in Sec. 3.1.3. This double pass is implemented by a concave mirror which reflects the light back inside the Fresnel rhomb and back inside the crystal. After reflection of the pump light back inside the crystal, there is again a probability to generate a vertically polarized photon pair. The position of the concave mirror is optimized in order to send the pump beam back inside the crystal along the same optical path as in the first pass. This double pass of the crystal generates a pair of down-converted photons in the first or in the second pass. The first pair is leaving the double pass with horizontal polarization, the second pair with vertical polarization. By adjusting the direction of polarization of the pump light, an equal superposition of horizontal and vertical generated pairs can be achieved. Since it is impossible in principle to predict if a photon pair was generated in the first or second pass (the coherence length of the pump laser also exceeds the length

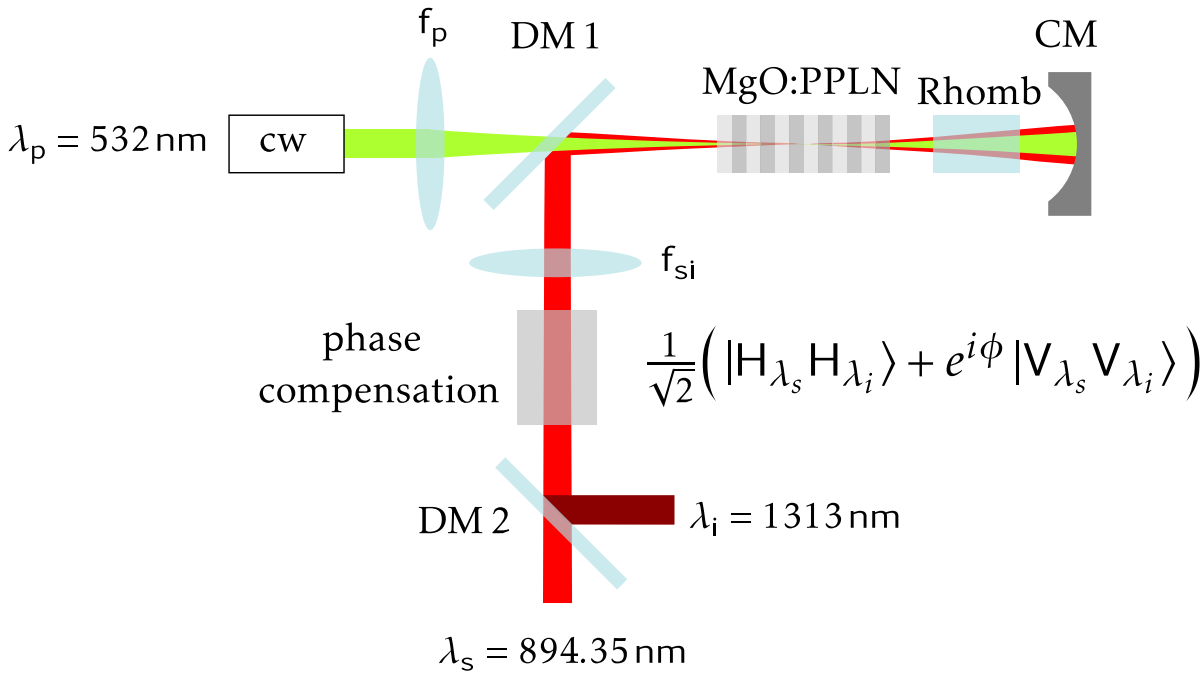

Fig. 3.1: Folded sandwich scheme [SRJ+13] for generating polarization-entangled photon pairs. It involves two dichroic mirrors DM, a concave mirror CM, two lenses with focal length $f_p = 100\,\mathrm{mm}$ for the pump photons with wavelength $\lambda_p = 532\,\mathrm{nm}$ and $f_{si} = 100\,\mathrm{mm}$ for the generated photon pairs with wavelengths $\lambda_s = 894.35\,\mathrm{nm}$ and $\lambda_i = 1313.1\,\mathrm{nm}$. For rotating the direction of polarization a Fresnel rhomb is used. Two crystals, a nonlinear crystal MgO:PPLN for down-conversion and a birefringent YVO4 crystal for phase compensation are in the setup. The pump source is a continuous wave (cw) diode laser.

of the folded configuration) the resulting state is the following:

$$|\psi\rangle = \frac{1}{\sqrt{2}}\left(|H_{\lambda_s}H_{\lambda_i}\rangle + e^{i\phi(\lambda_s,\lambda_i)}\,|V_{\lambda_s}V_{\lambda_i}\rangle\right) \tag{3.1}$$

By adjusting the phase $\phi(\lambda_s, \lambda_i)$, the resulting state can be one of the maximally entangled Bell-states $|\phi^+\rangle$ or $|\phi^-\rangle$. The tuning of the phase $\phi(\lambda_s, \lambda_i)$ is discussed in Sec. 3.1.4. For the separation of the generated photons from the pump photons a dichroic mirror DM1 is placed between the crystal and the lens f_p. Since this doesn't filter out all the pump photons, a longpass filter can be placed behind DM1. This may lead to lower noise on the detectors, since the pump photons could lead to false detections. In a second step the signal and idler photons are getting separated at another dichroic mirror DM2, the signal mode is then coupled into an optical fiber, coupling the photons to APD1, on the other arm, the idler mode gets coupled to APD2. The pump intensity is adjusted, so that only single pair events dominate the detection statistics. The output of APD1 is used to trigger the Indium Gallium Arsenide (InGaAs) APD2. A second plano-convex lens f_{si}, coated with respect to the non-degenerate wavelengths of the down-converted photons, is positioned in order to collimate the Gaussian collection mode with its beam waist assumed in the center of the down-conversion crystal. The position of this second lens with focal length $f_{si} = 100\,\mathrm{mm}$ is essential for an efficient coupling of the signal and idler modes to single mode fibers. For an efficient fiber coupling, the beam waists of the down-converted fields have to be matched to half of the mode field diameter for the respective fiber. The beam waists of the signal and idler photons can be estimated by a calculation of the pump beam waist. This calculation is fed by various measurements of the pump beam width behind the focusing lens f_p. Knowing the parameters of the pump beam and the setup, the waists of the signal and idler modes can be estimated, this will be discussed in section 3.3. The calculated beam width of the pump beam is shown in Fig. 3.2. This plot is the result of optimizing the positions of the optical components fulfilling two conditions. The first condition is equal beam waists in the first and the second pass, the second condition is that both beam waists are lying in the center of the crystal.

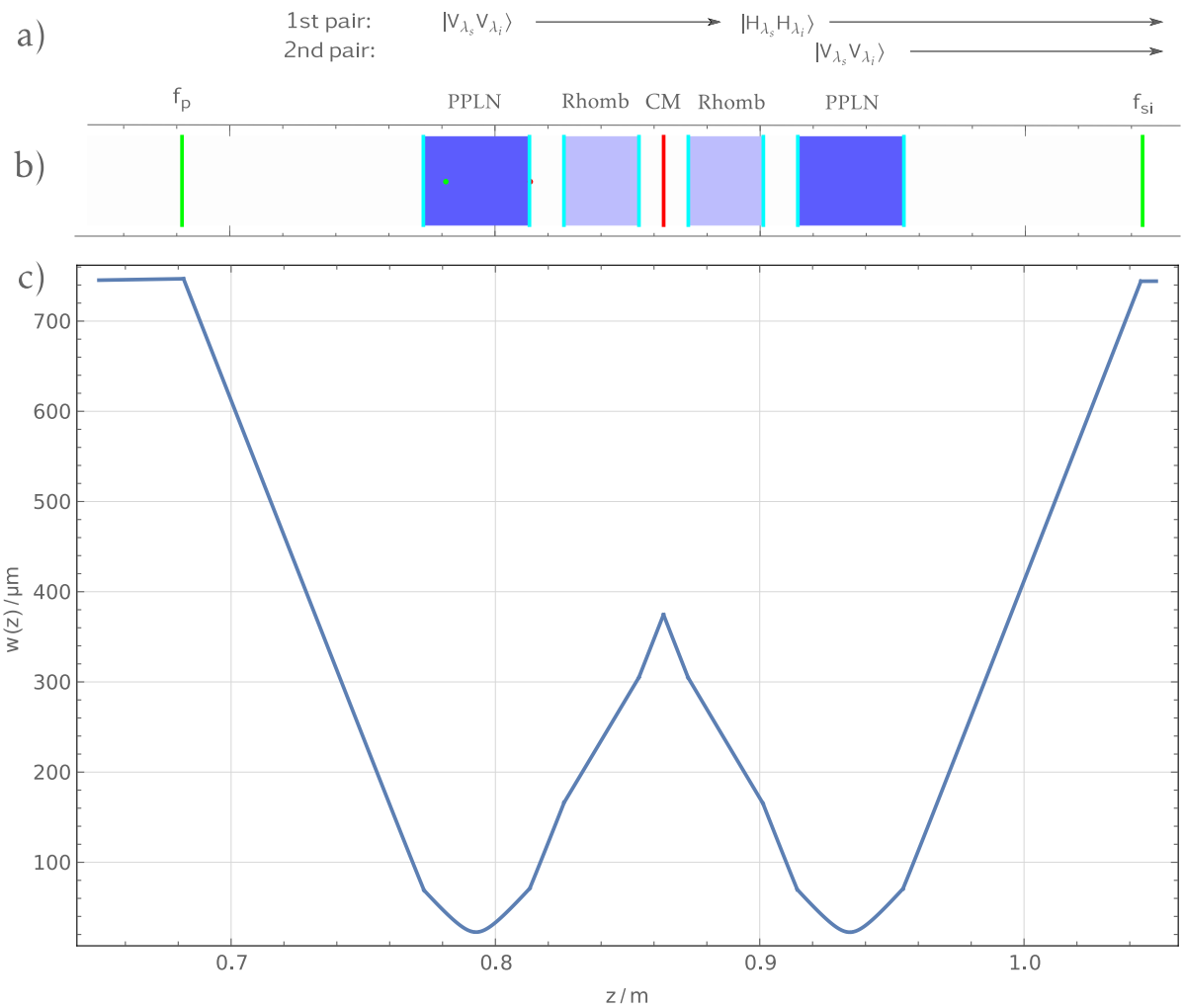

Fig. 3.2: Model of the the Folded Sandwich Configuration. The positions of the optical elements are shown in Fig. (b). In Fig. (c) the beam width of the pump beam is shown. The pump beam with a collimated beam width of approximately 750 µm is focused inside the MgO:PPLN down-conversion crystal using a plano-convex lens with focal length $f = 100\,\mathrm{mm}$. After passing the Fresnel rhomb, the light is reflected at a concave mirror and passes the nonlinear crystal a second time. The positions positions of the optical elements has been varied yielding the optimal values of $x_1 = 9.1\,\mathrm{cm}$ and $x_2 = 4.1\,\mathrm{cm}$. The resulting beam waist in each pass is 23 µm. In Fig. (a) the polarization states of the first and second pair is shown.

3.1.2 Down-Conversion in periodically poled lithium niobate

As already mentioned, in the process of spontaneous parametric down-conversion a pump photon, emitted by a diode pumped solid state laser (SLOC) with wavelength 532 nm and a specified bandwidth of 0.04 nm, splits into two lower energy photons at non-degenerate wavelengths, where the photon with lower wavelength is called the signal photon and the photon with higher wavelength is called the idler photon. The signal and idler photon has to be considered as a pair, created simultaneously in a small time window. Therefore, the detection of a signal photon heralds the existence of the corresponding idler photon. In Fig. 3.3 the calculated beam waist of the pump laser is plotted under the assumption of an incident collimated Gaussian beam and focal length $f_p = 100\,\mathrm{mm}$. Knowing the

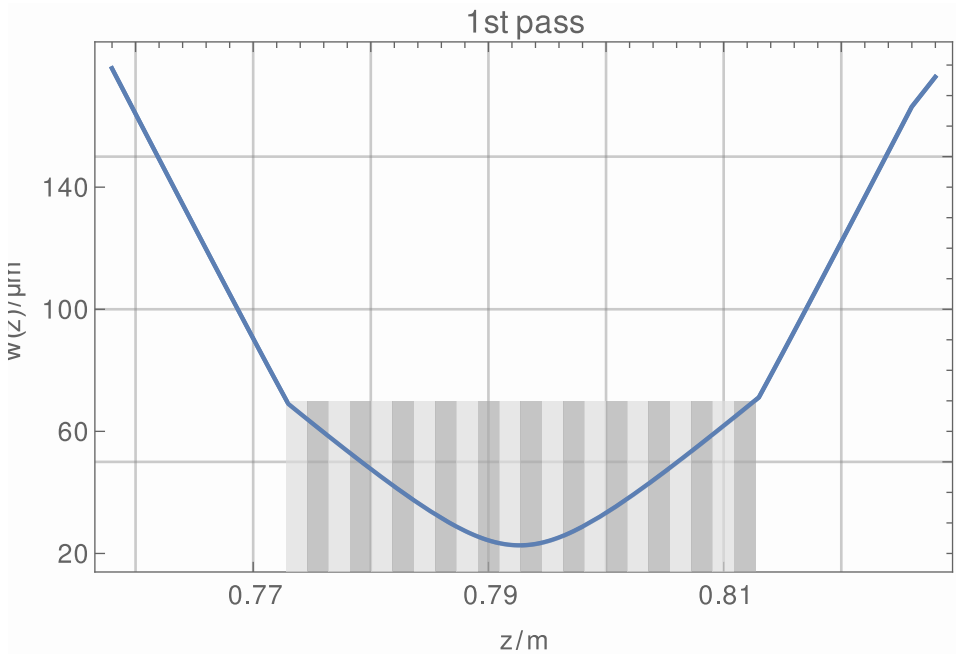

Fig. 3.3: Model of the Gaussian beam waist of the pump photons inside the nonlinear crystal. The focusing lens has focal length $f = 100\,\mathrm{mm}$, the optimal position of the waist is the center of the down-conversion crystal. The result is a waist of $w_0 = 23\,\mu\mathrm{m}$ with Rayleigh range $z_R = 3.0\,\mathrm{mm}$, giving a confocal parameter of $b = 6.0\,\mathrm{mm}$.

beam waist is important for calculating some properties of the down conversion and for designing an efficient coupling to single mode fibers. Clearly, of great importance for the experiment is a photon pair source with high brightness, therefore the confocal parameter of the pump photon with respect to the signal and idler photons has to be chosen appropriately. A detailed analysis will be discussed later. Beyond that, it is important to know that a pump source with a too large intensity can lead to the destruction of the down-conversion crystal. Assuming the above focusing with a beam waist of $w_0 = 750\,\mu\mathrm{m}$ incident on the lens $f_p = 100\,\mathrm{mm}$, destruction will not appear at pump powers below 1 W. The down-conversion process is phase matched using the technique of quasi-phase

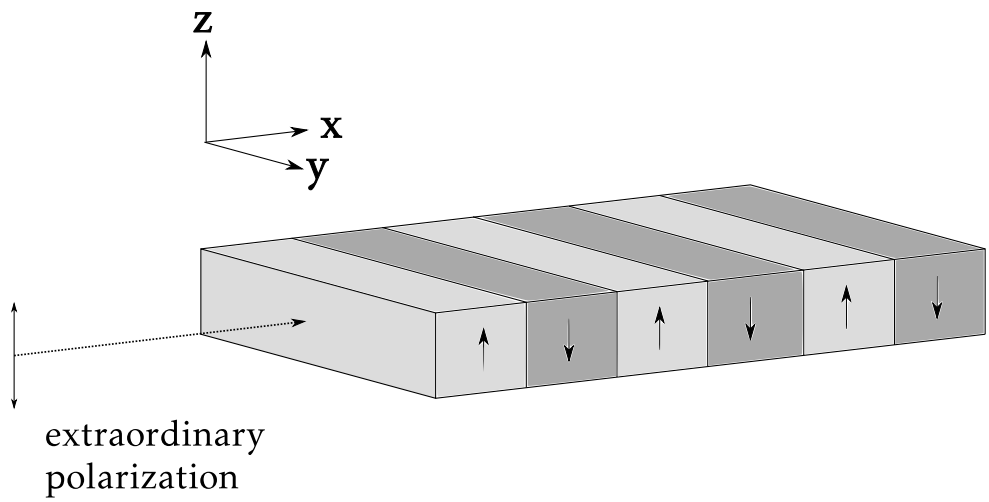

Fig. 3.4: Scheme of the MgO:PPLN down-conversion crysal. The pump photons are propagating along the x-axis. The nonlinear crystal is z-cut and the nonlinear optical coefficient d_{33} is reached using pump photons with vertical polarization. This direction corresponds to the extraordinary crystal axis, which is defined as the z-axis.

matching. The crystal consists of several different gratings with poling period in the range of 7 µm. For the desired application, the grating with poling period 7.0 µm is used which leads to a photon pair with $\lambda_{\text{signal}} = 894.35\,\text{nm}$ and $\lambda_{\text{idler}} = 1313.1\,\text{nm}$ at $T = 131.4\,°\text{C}$ with a given pump wavelength of $\lambda_{\text{pump}} = 532\,\text{nm}$. The crystal is cut, such that a vertical polarized pump photon is passing the extraordinary crystal axis. The down-converted signal and idler photons share the same vertical polarization along the extraordinary crystal axis. This type of phase-matching is known as type-0 phase-matching

$$\text{e} \rightarrow \text{e} + \text{e} \tag{3.2}$$

where all of the three interacting waves share the same state of polarization. While in the other known types, like type-I or type-II, at least one wave is polarized orthogonally with respect to the other waves. Type-0 phase matching allows all of the three interacting waves to propagate collinear. The corresponding nonlinear coefficient of lithium niobate is $d_{33} = 25\,\text{pm}\,\text{V}^{-1}$ [SKK+97], which is the highest coefficient for this type of material and also one of the highest coefficients known is only reachable by type-0 phase matching.

3.1.3 Fresnel Rhomb

The Fresnel rhomb is the important difference between the original folded sandwich scheme [SRJ+13] and this setup. In the original scheme, the rotation of the photons polarizations is implemented using an achromatic quarter-wave plate. Since in this setup the involved waves have large non-degeneracy in the order of 1000 nm a commercial quarter wave plate that has a retardance difference of about 0.2° (todo see Thorlabs?) are highly expensive. A nearly wavelength independent polarization rotator, known as a Fresnel rhomb is rotating the polarizations from vertical to horizontal. In the original setup, the solution is a specifically tailored wave plate, that introduces a half or full wave retardation on the 532 nm pump photons and a quarter wave retardation of the photon pairs in the near infrared.

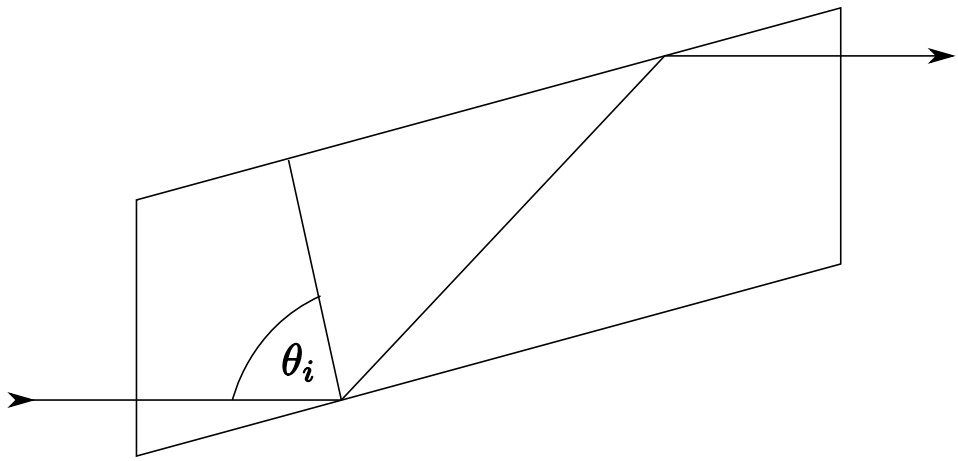

Fig. 3.5: Principle scheme of a Fresnel rhomb. Light incident under the angle θ_i is subject to total internal reflection. The two total internal reflections on the plan-parallel planes induce a phase shift $\Delta\phi$ between s- and p-polarized light. The calculated phase shift $\Delta\phi$ of the Fresnel rhomb is shown in Fig. 3.6, plotted over the angle of incidence.

The Fresnel rhomb is usually fabricated from a piece of glass with two plan-parallel surfaces, as depicted in Fig. 3.5. If the angle of incidence is greater than the critical angle

$$\theta_c = \arcsin\left(\frac{n_2}{n_1}\right) \tag{3.3}$$

total internal reflection occurs and light is reflected back inside the Fresnel rhomb. Under this circumstance the s- and p-polarized components of the incident beam of light are reflected back inside the rhomb while accumulating a relative phase shift. The refractive index n_2 is the refractive index of air and $n_1 = n_1(\lambda)$ is the refractive index of

glass (NBK7) [Mes08]. A single pass though the Fresnel rhomb, i.e. two total internal reflections, introduces a phase shift $\Delta\phi$ according to [BW99] of

$$\Delta\phi = \phi_s - \phi_p \tag{3.4}$$

$$= 2\arctan\left(\sqrt{\frac{\cos^2\theta_c}{\cos^2\theta_i} - 1}\right) - 2\arctan\left(-\frac{1}{\sin^2\theta_c}\sqrt{\frac{\cos^2\theta_c}{\cos^2\theta_i} - 1}\right) \tag{3.5}$$

as can be seen in Fig. 3.6 for the two relevant wavelengths $\lambda_{\text{signal}} = 894.35\,\text{nm}$ and $\lambda_{\text{idler}} = 1313.1\,\text{nm}$ over different angle of incidences θ_i. For a linearly polarized incident beam of light, oriented at 45°, the Fresnel rhomb is acting as a wavelength independent quarter wave plate. The first reflection introduces a phase shift of 45° transforming a linear polarization to an elliptical and the second reflection transforms the elliptical polarization to circular polarization. In the setup, the rhomb is oriented at 45° with respect to the vertical polarization direction of the photon pair emitted in the first pass. The Fresnel rhomb transforms the vertical pair, after double pass of the rhomb and a reflection at the concave mirror, to horizontal polarization, while the polarization of the diagonally polarized pump photon stays the same. The Fresnel rhomb is cut for an angle of incidence of 54.8°.

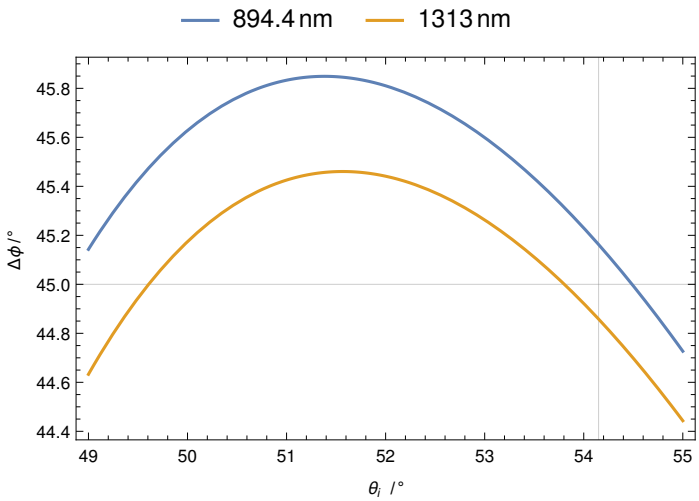

Fig. 3.6: Plot of the phase shift $\Delta\phi$ induced by total internal reflection in a Fresnel rhomb over the angle of incidence θ_i. For the calculation of $\Delta\phi(\theta_i, n_2(\lambda))$ the wavelength-dependent refractive index of N-BK7 was used.

3.1.4 Phase Compensation

A key requirement for the generation of entangled photon pairs is the production of indistinguishable photons in the first and in the second pass of the pump beam. In the folded sandwich scheme the first and the second pair of photons are subject to different dispersion. The second pair is only propagating along the extraordinary axis of the nonlinear crystal for a distance of half its length. The first pair is propagating along the extraordinary axis for the same distance, in addition, this pair is passing various optical elements. It is passing the Fresnel rhomb two times and after reflection it is propagating along the ordinary crystal axis of the nonlinear crystal for its whole length. To generate polarization entangled photon pairs, the task is to compensate the chromatic dispersion acquired by the two pairs. Due to the large non-degenerate wavelengths, 894.35 nm for the signal photons and 1313.1 nm for the idler photons, this is a challenging task. The first pair accumulates the following phase relative to the second pair

$$\begin{aligned}\phi(\lambda_s, \lambda_i) = L_{PPLN} &\left(\frac{n^{(o)}_{PPLN}(\lambda_s, T)}{\lambda_s} + \frac{n^{(o)}_{PPLN}(\lambda_i, T)}{\lambda_i} \right) + \\ &+ 2L_{RHOMB} \left(\frac{n_{BK7}(\lambda_s)}{\lambda_s} + \frac{n_{BK7}(\lambda_i)}{\lambda_i} \right)\end{aligned} \tag{3.6}$$

this relative phase is plotted in Fig. 3.7 over the wavelength of the signal and idler photons. This information can lead to in principle distinguishable photons and a deterioration of entanglement. By placing a birefringent compensation crystal between DM1 and DM2, introducing the inverse dispersive characteristics, this distinguishing information can be erased.

For compensation of the different phases accumulated, a crystal made out of yttrium orthovanadate (YVO4) is used. The first pair is sent through the extraordinary crystal axis, while the second pair is sent through the crystal with its polarizations oriented along the ordinary crystal axis. To compensate the phase difference with the compensation crystal, where the length L_{YVO_4} can be chosen freely, such that

$$\phi_C(\lambda_s, \lambda_i) = L_{YVO_4} \left(\frac{n^{(o)}(\lambda_s)}{\lambda_s} + \frac{n^{(o)}(\lambda_i)}{\lambda_i} - \left(\frac{n^{(e)}(\lambda_s)}{\lambda_s} + \frac{n^{(e)}(\lambda_i)}{\lambda_i} \right) \right) \tag{3.7}$$

yields a flat phase for 894.35 nm and 1313.1 nm, i.e.,

$$\phi(\lambda_s, \lambda_i) + \phi_C(\lambda_s, \lambda_i) \approx C$$

$$\frac{\mathrm{d}}{\mathrm{d}\lambda} (\phi + \phi_C) \Big|_{\lambda_s, \lambda_i} \approx 0$$

As can be seen in Eq. (3.8), a constant offset is not relevant, since we are only interested in making the signal and idler photons of the two pairs indistinguishable. The

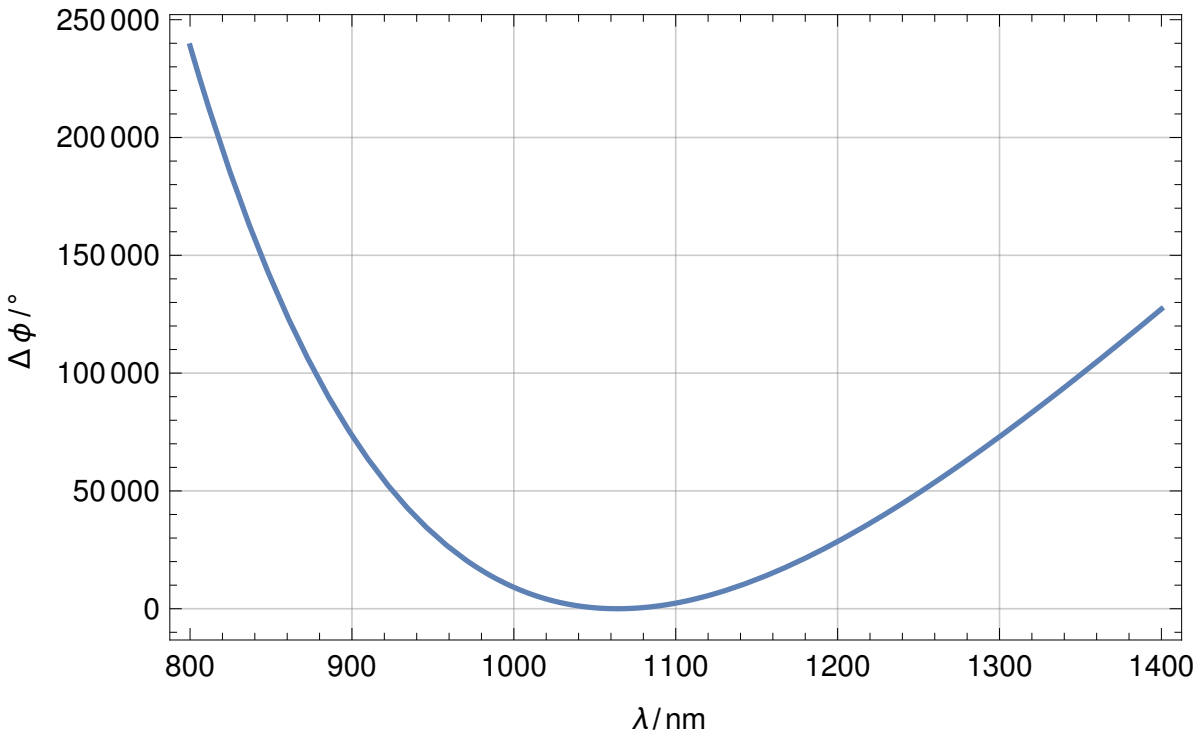

Fig. 3.7: Relative phase of the signal and idler photons after the double pass in the folded sandwich scheme (see Fig. 3.1 or Fig. 3.2).

absolute phase is not relevant for this application. Introducing a flat relative phase is leading to indistinguishable photon pairs. Using various different Sellmeier equations of yttrium orthovanadate (see Sec. A.2) results in different optimal lengths for the compensation crystal, dependent on the given Sellmeier equation. The resulting lengths are the following

$$L_{YVO4} = 138.3\,\mathrm{mm} \quad \text{(from [foc14])} \tag{3.8}$$
$$L_{YVO4} = 172.0\,\mathrm{mm} \quad \text{(from [ST14])} \tag{3.9}$$
$$L_{YVO4} = 154.0\,\mathrm{mm} \quad \text{(from [ZLC}^{+}\text{10])} \tag{3.10}$$

In Fig. 3.8 and Fig. 3.9b the relative phase of signal and idler photons after the double pass and after pass through the compensation crystal is shown for the length given in Eq. (3.9).

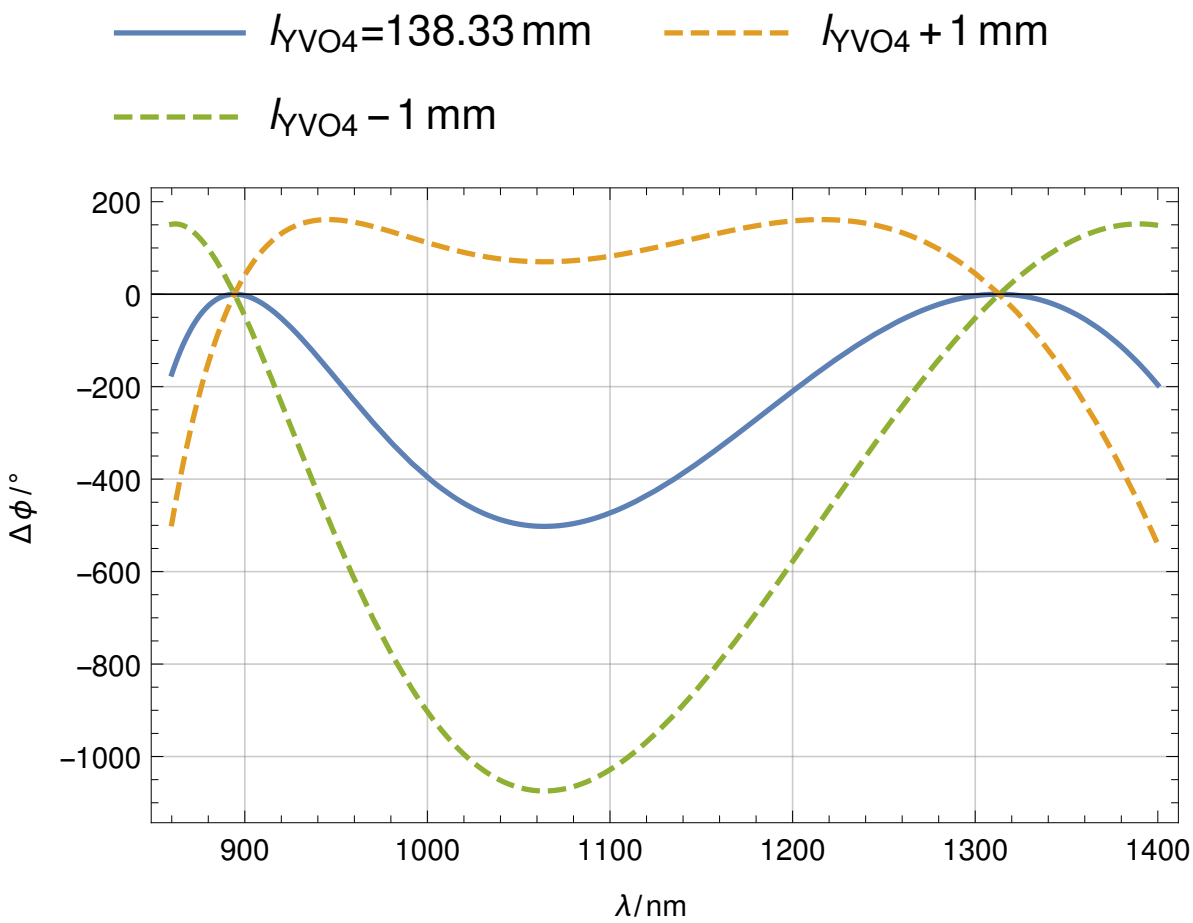

Fig. 3.8: Relative phase of the signal and idler photons after double pass and compensation crystal. The Sellmeier equation for YVO4 was taken from [foc14].

In Fig. 3.9a and Fig. 3.9b a closer look at the relative phase for the two relevant wavelength ranges is shown.

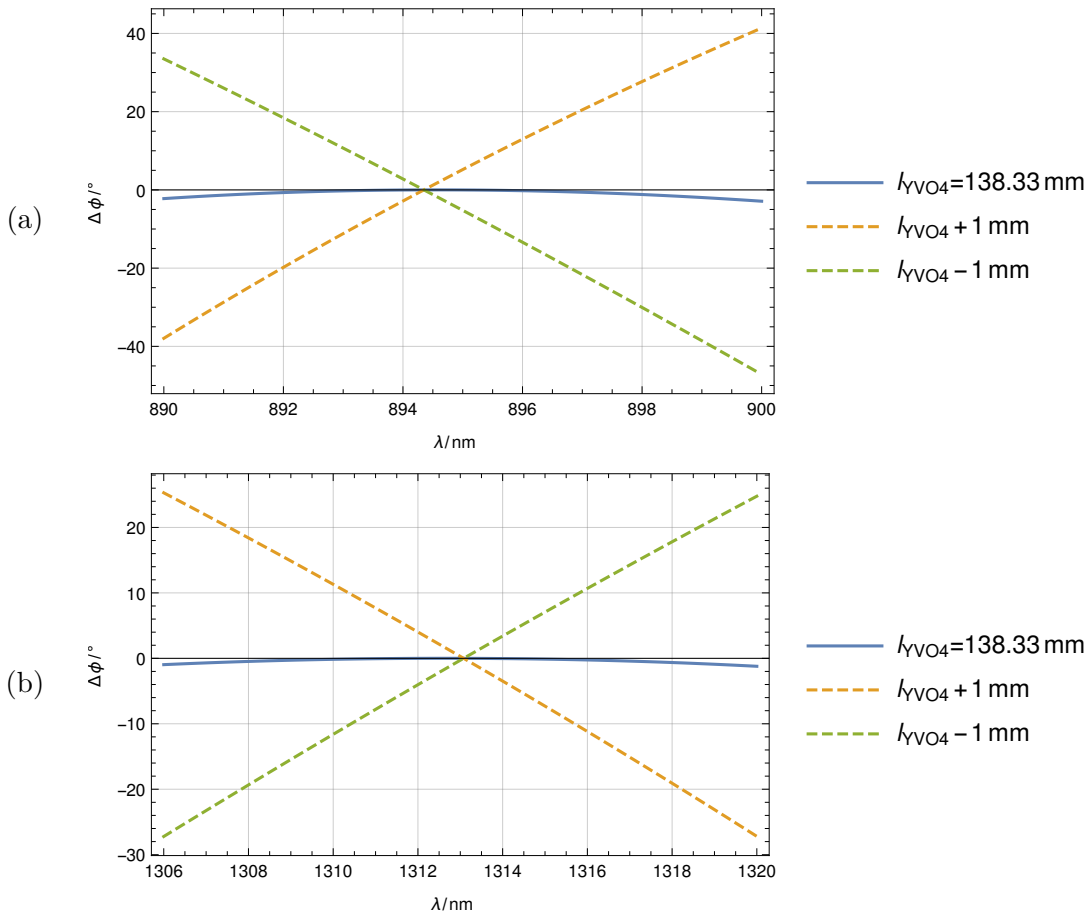

Fig. 3.9: Closer look at the relative phase in the relevant wavelength ranges. The optimal length of the compensation crystal is shown together with a variation of ± 1 mm shown in dashed. The relative phase in the range of the signal photons is shown in (a), the relative phase in the range of the idler photons is shown in (b).

3.2 Filtering quantum light with a Czerny-Turner spectrograph

In addition to a tunable light source a tunable filter is required. The Czerny-Turner spectrograph is a common optical system for analyzing the spectral properties of a light source. In the setup the Czerny-Turner spectrograph is used to analyze the spectral properties of the down-converted light.
A spectral filter can be implemented by spatially filtering the output of the spectrograph. In this operation mode the spectrograph is called a monochromator. Working in 0th order, the spectrograph is mapping the entrance slit onto the exit slit. In higher orders, different wavelengths are sent into different directions, caused by the dispersing element. In case of a Czerny-Turner spectrograph, the dispersive element is a grating structure.
The output of the spectrograph can be recorded using a camera, mounted at the exit slit. In order to filter light spectrally, the output can be spatially filtered by changing the width of the exit slit. A given slit width at a fixed distance relative to the grating corresponds to a spectral bandwidth $d\lambda/dx$. This bandwidth is dependent on the grating structure, i.e. it's frequency. With a given grating frequency $g = d^{-1}$, the spectral bandwidth at the output is determined by the width Δx of the exit slit. For an ideal monochromatic wave at the exit slit of width

$$\Delta x = f\,\frac{\lambda}{W} \tag{3.11}$$

with W being the illuminated width of the grating, f being the focal length of the focusing optics and λ the wavelength of the monochromatic light source. This results in a minimum entrance slit width of

$$b > 2\,f\,\frac{\lambda}{W} \tag{3.12}$$

The entrance slit should be opened as wide as possible to collect the light efficiently. On the other hand, in order to minimize stray light, the slit should be not wider than the laser beam width and the above condition should be fulfilled. For a monochromator, the width of the exit slit determines the bandwidth of the transmitted spectrum.

Calculation of the path difference at the grating

In Fig. 3.10 the relevant lengths and angles are defined, the relevant quantities are

α	Angle between grating normal and incoming ray
β	Angle between grating normal and diffracted ray
$\vec{n}$	grating normal
λ	wavelength
d	grating
$g = d^{-1}$	grating frequency
$s_{1,2}$	Path difference

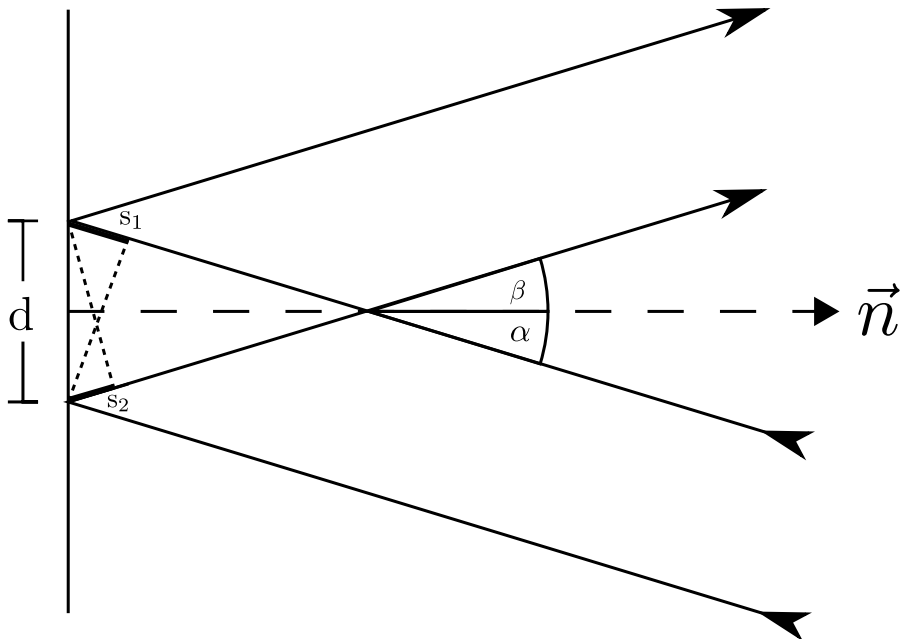

Fig. 3.10: Optical path difference $\Delta s = s_1 - s_2$ at grating with frequency d.

The optical path difference introduced by the grating structure is therefore

$$\Delta s = s_2 - s_1 \tag{3.13}$$

$$= d(\sin\beta - \sin\alpha) \stackrel{!}{=} n\lambda \tag{3.14}$$

$$\Leftrightarrow \sin\beta - \sin\alpha = n\lambda g \tag{3.15}$$

Calculation of the angular and spectral dispersion

The relevant optical path inside the Czerny-Turner spectrograph is depicted in Fig. 3.11. After focusing on the entrance slit, the light is sent to a spherical mirror that collimates the light. The parallel rays are then incident on the grating and get reflected in all directions. A part of the reflected light gets focused using another spherical mirror to focus the light onto the exit slit or the chip of a camera. In case of grating position $\varphi = 0$, the angle of the incoming ray α is equal the angle of the out going ray β, and in addition equals the so called half angle ϵ that has the constant value $\epsilon = 8.58° = \text{const}$. The relevant quantities are

ϵ	half angle
φ	grating rotation
$\vec{n}_0$	grating normal at $\varphi = 0$
f	focal length

the path difference at the grating is

$$\sin\alpha + \sin\beta = n\lambda g \tag{3.16}$$

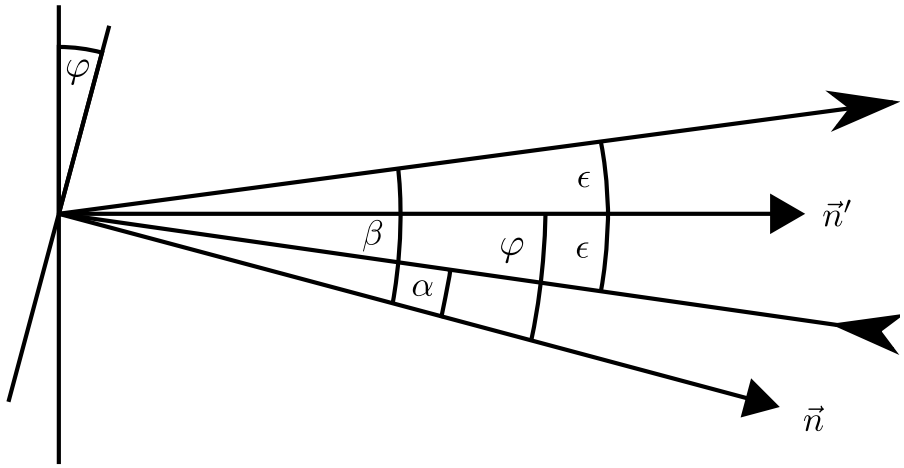

Fig. 3.11: Optical path at the grating inside of the Czerny-Turner spectrograph.

since the angle α is taken to be negative, in comparison with equation 3.15. From Fig. 3.11 one gets

$$\alpha = \varphi - \epsilon \tag{3.17}$$
$$\beta = \varphi + \epsilon \tag{3.18}$$

this yields

$$\sin(\varphi - \epsilon) + \sin(\varphi + \epsilon) = n\lambda g \tag{3.19}$$
$$2\sin(\phi)\cos(\epsilon) = n\lambda g \tag{3.20}$$
$$\Rightarrow\ \varphi = \arcsin\left(\frac{n\lambda g}{2\cos\epsilon}\right) \tag{3.21}$$

With this result one can calculate the grating rotation φ for a given center wavelength. Calculation of the angular dispersion

$$\frac{\mathrm{d}\lambda}{\mathrm{d}\beta} = \frac{\mathrm{d}}{\mathrm{d}\beta}\left(\frac{1}{ng}\left(\sin\alpha + \sin\beta\right)\right) = \frac{1}{ng}\cos\beta \tag{3.22}$$
$$\tag{3.23}$$

The angular dispersion is a measure for the wavelength dispersion behind the grating. The spectral bandwidth in the focal plane of the spherical mirror, focusing on the exit slit is according to 3.12

$$\boxed{\frac{\mathrm{d}\lambda}{\mathrm{d}x} \approx \frac{\cos\beta}{fng} = \frac{\cos\left(\epsilon - \varphi\right)}{fng}} \tag{3.24}$$

since

$$\frac{\Delta x}{f} = \tan(\Delta\beta) \overset{\Delta\beta \ll 1}{\approx} \Delta\beta \quad \text{und} \quad \frac{\mathrm{d}\lambda}{\mathrm{d}\beta} \approx f^{-1}\frac{\mathrm{d}\lambda}{\mathrm{d}x} \tag{3.25}$$

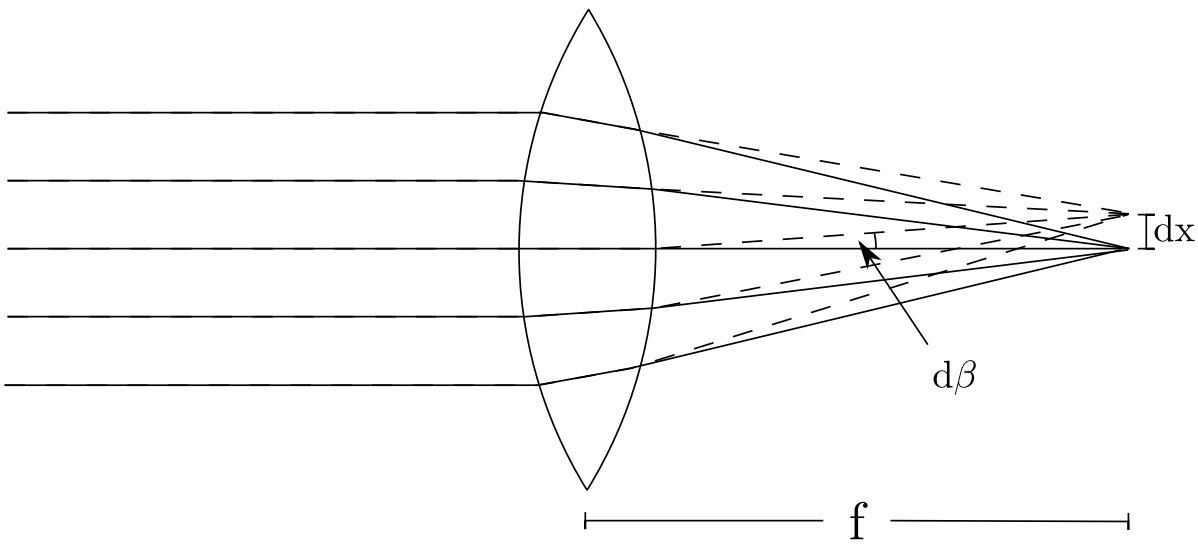

Fig. 3.12: Focusing of the collimated light onto the exit slit of the Czerny-Turner spectrograph.

Numerical Values for the spectral bandwidth

In Table 3.1 is the summarized result of calculating the spectral bandwidth for light at wavelength $\lambda = 894.35\,\mathrm{nm}$ and three different gratings.

grating frequency (mm)	$\lambda_{\mathrm{center}}$ (nm)	spectral bandwidth (nm / mm)
600	894.35	3.04
1200	894.35	1.25
1800	894.35	0.50

Table 3.1: Calculated values of the spectral bandwidth for three different gratings.

3.3 Single Mode Coupling

Essential for an efficient source with high brightness is an optimal coupling from the source to the detectors. The highest brightness in coupling to fibers can be reached by multi-mode fibers. The use of multi-mode fibers can lead to distinguishing information between the first and the second pass. This spatial information can effectively erased by projection into the Gaussian mode of a single-mode fiber. The coupling of the down-converted light is implemented by the use of single mode fiber for the signal mode and a respective fiber for the idler mode. The fundamental mode of a single-mode fiber has a nearly Gaussian profile. For reaching a high coupling efficiency, the Gaussian light beam has to be focused such that the beam waist equals the mode radius of the respective fiber. By varying the position of the fiber end around the beam waist one can find an optimal alignment of the fiber relative to the incoming light beam which leads to an optimal coupling. In general, the condition for single-mode guidance is

$$V = \frac{2\pi}{\lambda} a \sqrt{n_{\text{core}}^2 - n_{\text{cladding}}^2} < 2.405 \tag{3.26}$$

where a is the core radius, n_i are the refractive indexes of core and cladding and λ is the transmitted wavelength. Equation (3.26) defines the cut-off wavelength, that is the wavelength above which the fiber has single-mode guidance. Considering the setup, a standard SMF28 fiber with cutoff wavelength 1254 nm was chosen for the idler mode and a SM800 fiber with cutoff wavelength 800 nm for the signal mode. The next step is to choose the right collimation optics. The beam widths of the relevant modes were calculated using Gaussian transfer matrix formalism. The beam width of the pump beam is shown in Fig. 3.2 with the optimal positions of the involved optical elements in order to achieve the same waist in the first as in the second pass of the down-conversion crystal.

The beam widths of all participating waves are shown in Fig. 3.13. Important parameters for finding the right collimation optics are the beam widths of the signal and idler modes after getting collimated by the lens f_{si}. In case there is no suitable stock items, the respective beam waist can be transformed using a lens system. This was done for the signal mode, as can be seen in Fig. 3.13.

The optimal focusing parameters were calculated with the condition of Boyd and with the condition of Bennink for a fixed pump waist. The condition of Boyd [Boy08] leads to

$$w_p = 23.0\,\mu\text{m},\ w_s = 30.2\,\mu\text{m and } w_i = 36.8\,\mu\text{m} \tag{3.27}$$

Assuming a fixed pump waist of 24.9 µm the condition of Bennink leads to

$$w_s = 31.5\,\mu\text{m and } w_i = 38.3\,\mu\text{m} \tag{3.28}$$

For calculating the single-mode coupling the results according to Bennink [Ben10] were used.

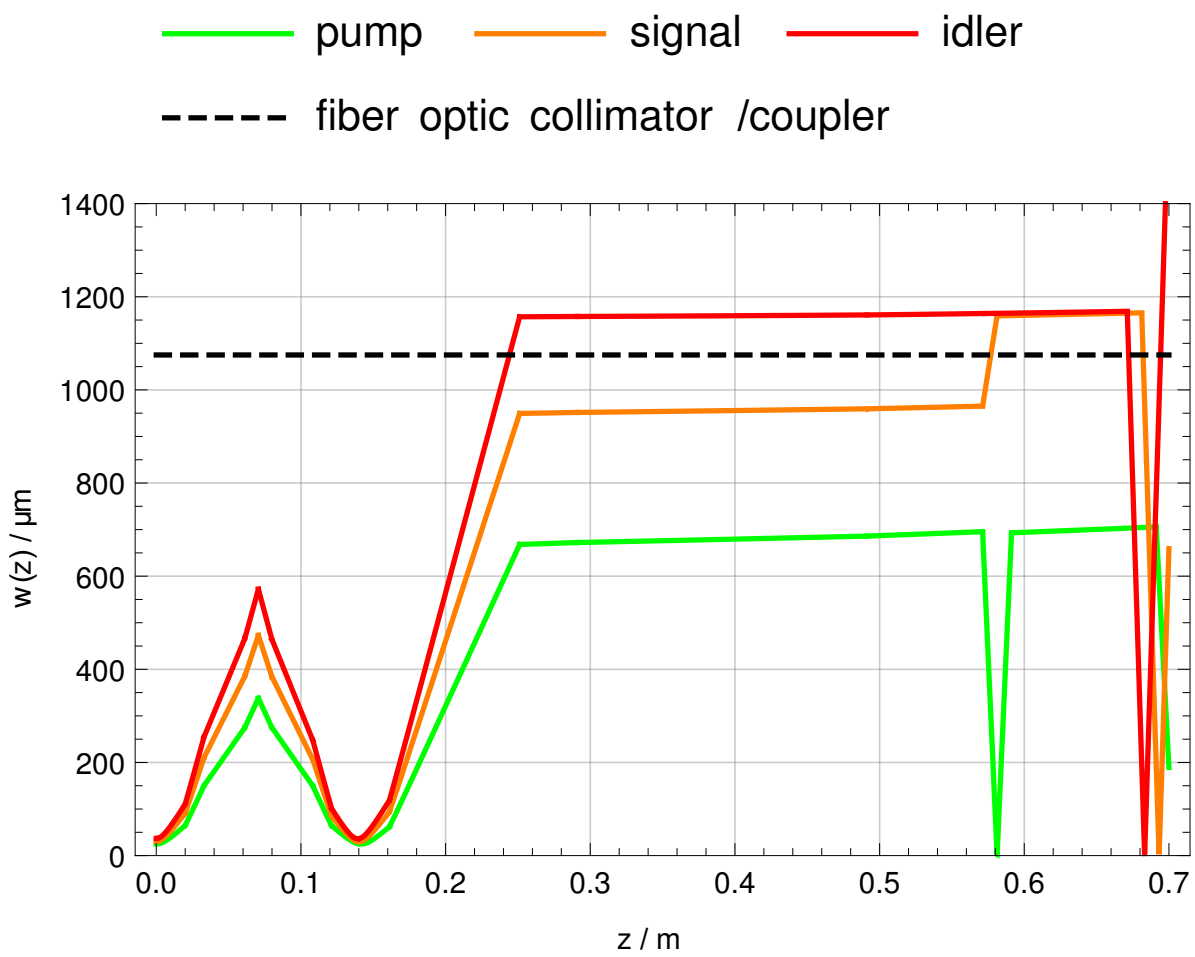

Fig. 3.13: Calculated beam widths of all three involved waves in order to find optimal coupling conditions to single mode fibers. The generated waves are assumed to start in the center of the crystal during the first pass. The assumed beam waists at the center of the crystal $z = 0\,\mathrm{m}$ are $w_{0,pump} = 25\,\mu\mathrm{m}$, $w_{0,signal} = 32\,\mu\mathrm{m}$ and $w_{0,idler} = 39\,\mu\mathrm{m}$. These values are taken from Eq. (3.28). As a result, one gets the optimal position $z = 25\,\mathrm{cm}$ for the collimating, near-infrared lens and the optimal lens system for the coupling to single-mode fibers. The lens system in the signal arm at position $z = 0.58\,\mathrm{m}$ consists of two lenses, one with focal length $f_A = -50\,\mathrm{mm}$, the other with focal legth $f_B = 60\,\mathrm{mm}$.

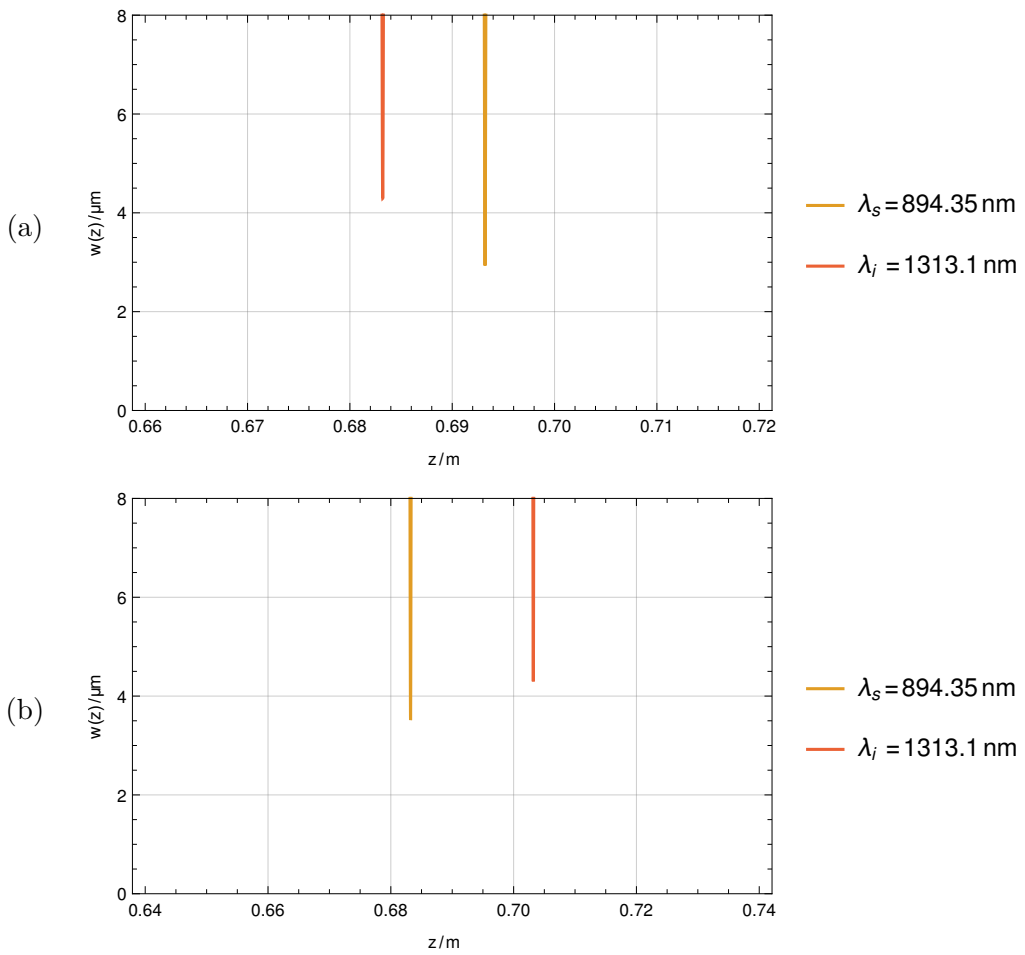

Fig. 3.14: Calculated beam waists at the fiber tip. The mode field diameter of the the fibers are specified with $MFD_{SM800} = 5.6\,\mu\text{m}$ and $MFD_{SMF28} = 9.2(4)\,\mu\text{m}$. An estimation of the resulting coupling efficiencies is given in Sec. 4.4.

3.4 Detectors

For the detection of single photons two kind of detectors have been used. Avalanche photo diodes (APD) and superconducting single photon detectors (SSPD). Both detectors allow the detection of single photons.

3.4.1 Single-photon avalanche diode

An avalanche photo diode converts light to electricity. The avalanche photo diode is a semiconductor device based on a p-n junction. For an incident photon creating an electron-hole pair, the free electron gets accelerated and triggers an avalanche of electrons. In this work an APD based on silicon and an APD based on InGaAs were used.

3.4.2 Superconducting single photon detector

The superconducting single photon detector is based on a current-biased superconducting nanowire cooled below its critical temperature. An incident photon breaks Cooper pairs and a measurable voltage pulse is produced. Most SSPDS are made out of niobium nitride, a material with a relatively high critical temperature of about 10 K.

3.5 Gated coincidence measurements

The production of single photon states and correlated pairs in a controlled and deterministic way, is a challenging task. SPDC photon pair sources are not inherently deterministic, however, combining a heralded single photon source with a quantum memory, i.e. a device that can store and emit photons in a deterministic way, it is possible to implement an on-demand single photon source [RMG+13].

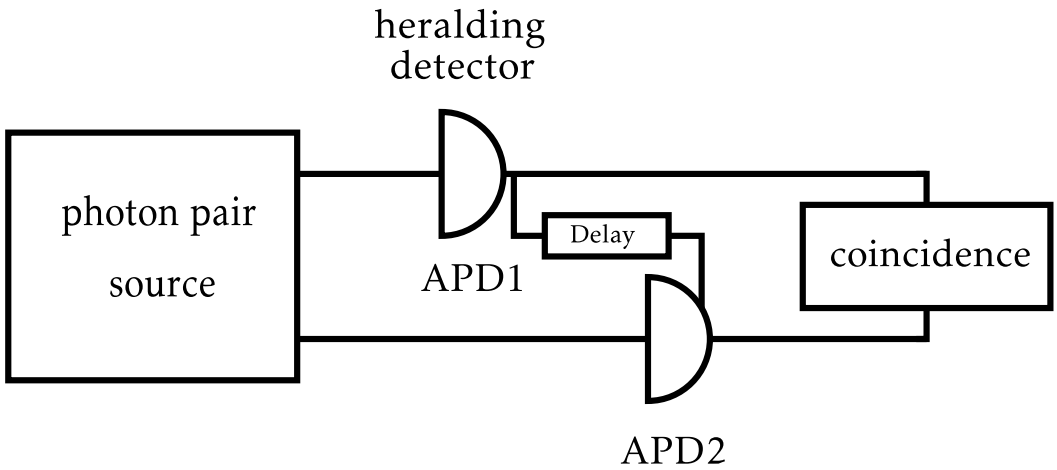

Fig. 3.15: Scheme of the gated coincidence measurements. A photon pair source emits a pair of photons, a click on the detector in the upper mode heralds a single photon in lower mode. By adjusting the delay, the gate of APD2 is only opening its gate when an incoming photon of a pair is incident. This trigger scheme can lead to a strongly reduced noise in coincidence measurements.

The basic scheme of the gated coincidence measurements is shown in Fig. 3.15. The photon pair source is based on a bi-directionally pumped MgO:PPLN crystal. The emission is separated into two different spatial modes, separating the wavelengths into a signal and an idler mode. Both emissions are then coupled to single-mode fibers. The signal mode serves as the heralding arm, a click on APD1 heralds the presence of a photon in the idler arm. Detector APD2 in the idler arm has a relatively high noise level. In contrast to APD1, the idler detector APD2 can be operated in a gated mode. Coincidence measurements were performed when APD2 is run in the triggered mode. By adjusting the delay of the triggered APD2 placed in the idler arm and by choosing a short gate window τ_{gate}, one can in principle achieve a heralding detection efficiency

limited mainly by the quantum efficiencies of the avalanche photo diodes APD1 and APD2. A coincidence is defined as the detection of two photons, one in the signal arm and another in the idler arm within the gate window τ_{gate}. With the rate of the produced pairs R_0 and the detector efficiencies η_i one can write equations for the ideal singles rates in each arm

$$S_1 = R_0\eta_1 \tag{3.29}$$
$$S_2 = R_0\eta_2 \tag{3.30}$$

given a value of about

$$R_{\text{cc}} = R_0\eta_1\eta_2 \tag{3.31}$$
$$\approx 0.1R_0 \tag{3.32}$$

3.6 Tuning of the relative phase using a crystal oven

For generating one of the two Bell states $|\phi^+\rangle$ or $|\phi^-\rangle$, the phase has to be set to $\phi = 0$ or $\phi = \pm\pi$ (see Eq. (2.48) and (2.47)). To this end, a crystal oven (see Fig. 3.16) was designed and manufactured for heating the YOV4 compensation crystal, and therefore adjusting the phase of the photon pairs.
The crystal oven consists of a copper case, that is fixing the compensation crystal and also serves as a heat contact between the crystal and the heating element, the Peltier element. A difficulty is that the opposite side of the Peltier element, which in this application is the cooler side, has to be isolated from the warm side. The Peltier element is controlled using a commercial PID controller.

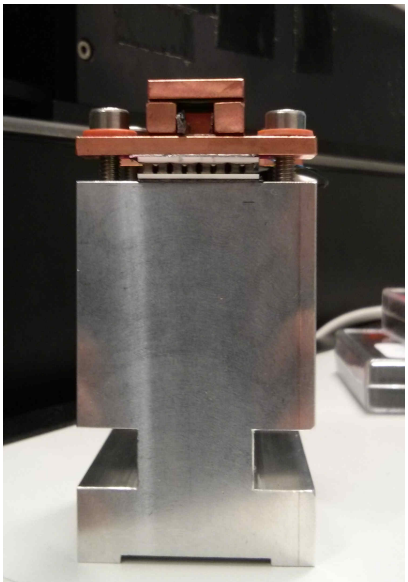

Fig. 3.16: Peltier oven for crystals with 4 cm length and an aperture of 5 mm x 5 mm.

3.7 Polarization correlations

The folded sandwich scheme generates entangled photon pairs (see Sec. 3.1). The continuous wave pump laser produces a superposition of the states $|H_s H_i\rangle$ and $|V_s V_i\rangle$, which can in general be written as

$$|\psi\rangle = \alpha\,|H_s H_i\rangle + \beta e^{i\phi}\,|V_s V_i\rangle \tag{3.33}$$

By setting $\alpha = \beta = \frac{1}{\sqrt{2}}$ and $\phi = 0$, the source can be used to generate a maximally entangled Bell state.
By measuring the correlations in the photon pairs polarization states one can show that the entanglement exists between the generated pairs of signal and idler photons. The detection setup is shown in Fig. 3.17

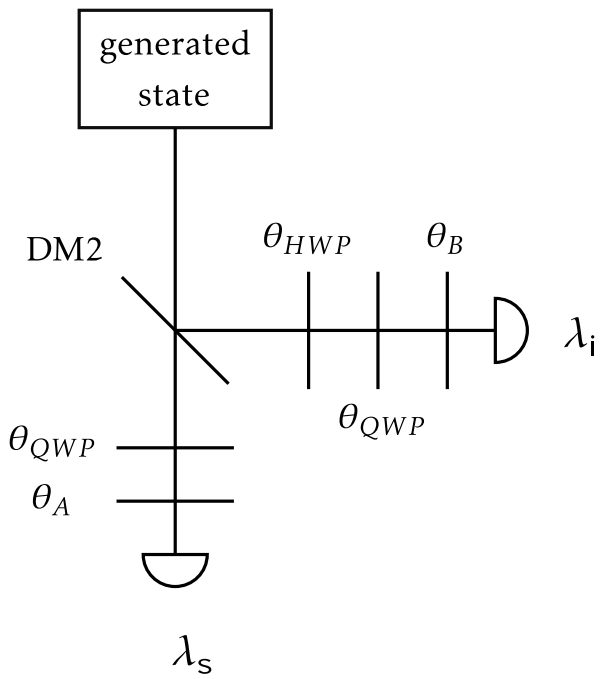

Fig. 3.17: Setup of the correlation measurement. A polarizer with angle setting θ_A was placed in the signal arm and a polarizer with angle setting θ_B is placed in the idler arm. For some measurements, in addition, quarter wave plates and half wave plates were introduced in each arm for controlling the polarization. The detectors used were the silicon APD1 for the signal arm and the InGaAs APD2 for the idler mode.

To test for entanglement, a joint polarization state measurement must be made in two non-orthogonal polarization bases (see Sec. 2.2.5). Considering the source of polarization entangled photon pairs, producing horizontal or vertical pairs of photons, an appropriate choice of basis is the horizontal/vertical basis with states ($|H\rangle\,/\,|V\rangle$) and the diagonal/antidiagonal basis with states ($|D\rangle\,/\,|A\rangle$).

The setup of two polarizers A and B with their transmission axis aligned to the vertical with the angles θ_A and θ_b the probability of measuring two photons of a pair in the maximally entangled Bell-state is

$$P(\theta_A, \theta_B) = \left|\langle \theta_A \theta_B | \phi^+ \rangle\right|^2 \tag{3.34}$$

$$= \frac{1}{2}\Big(1 - V \sin(\theta_A - \theta_B)\Big) \tag{3.35}$$

The expected quantum mechanical correlations of various two-photon states and an incoherent mixture are shown in Fig. 3.18, Fig. 3.19 and Fig. 3.20. The measurement basis VV represents a measurement with both polarizers oriented vertical, i.e. $\theta_A = 0°$ and $\theta_B = 0°$. The R and L bases represent a measurement where a quarter wave plate is introduced in the respective arm. In Table 3.2 the various measurement bases used for the calculation of the probabilities are shown.

basis	signal arm		idler arm	
	θ_A	θ_{QWP}	θ_B	θ_{QWP}
VV	0	-	0	-
HH	90	-	90	-
DD	45	-	45	-
AA	315	-	315	-
RR	0	-45	0	-45
LL	0	45	0	45

Table 3.2: Orientations of the optical elements in the calculations shown in Fig. 3.18, Fig. 3.19 and Fig. 3.20.

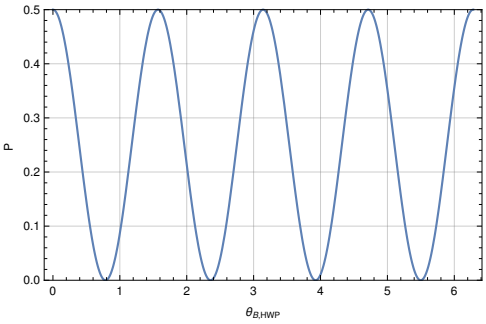

(a) VV

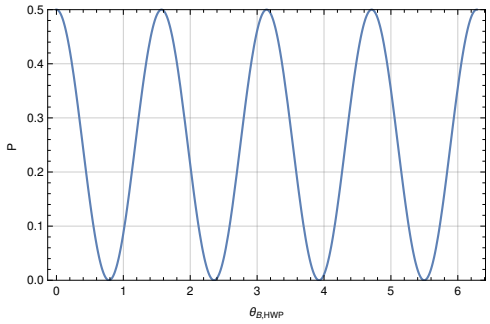

(b) HH

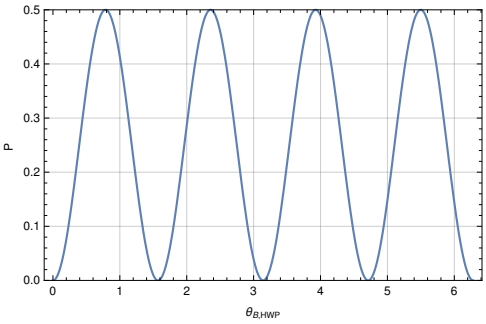

(c) DD

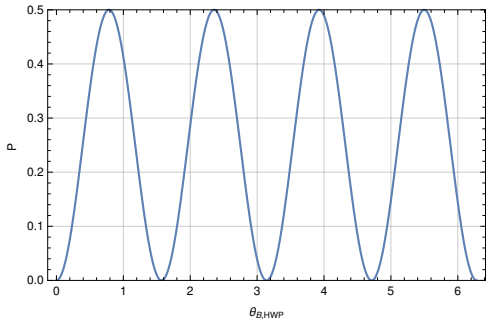

(d) AA

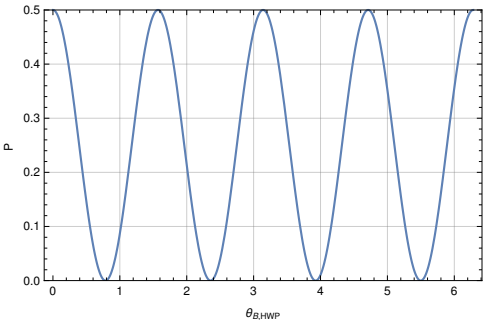

(e) LL

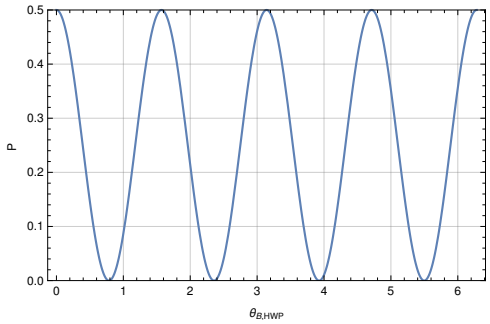

(f) RR

Fig. 3.18: Probabilities of the state $|\phi^-\rangle$ in various measurement bases (Table 3.2) plotted over the angle of the half-wave plate θ_{HWP} in the idler arm. The fidelity of this state using Eq. (2.80) and Eq. (2.81) is $F = 1$.

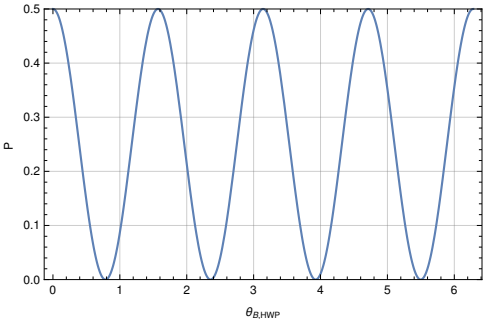

(a) VV

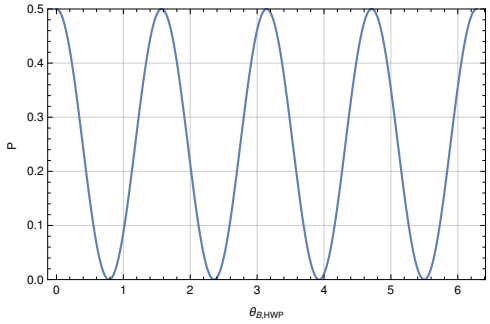

(b) HH

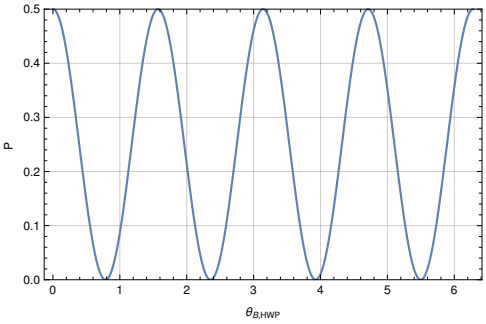

(c) DD

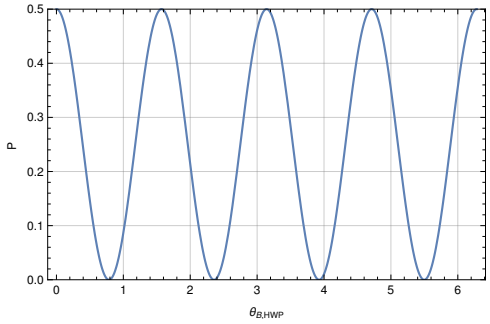

(d) AA

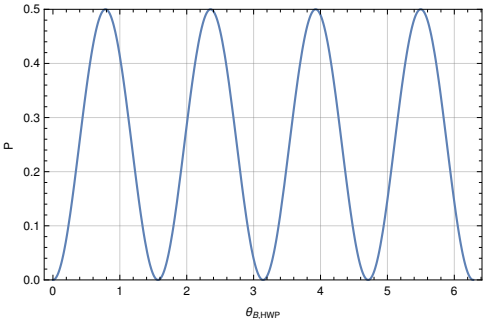

(e) LL

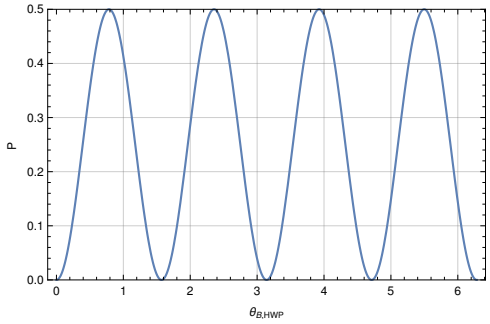

(f) RR

Fig. 3.19: Probabilities of the state $|\phi^+\rangle$ in various measurement bases (Table 3.2) plotted over the angle of the half-wave plate θ_{HWP} in the idler arm. The fidelity of this state using Eq. (2.80) and Eq. (2.81) is $F = 1$.

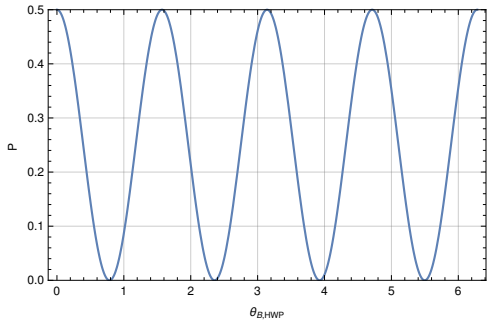

(a) VV

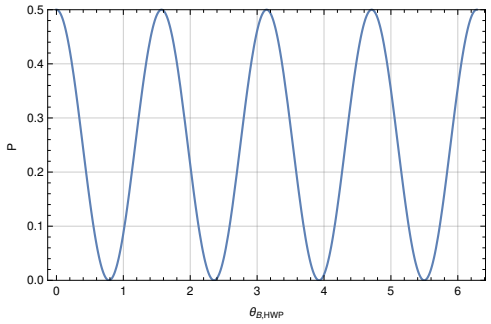

(b) HH

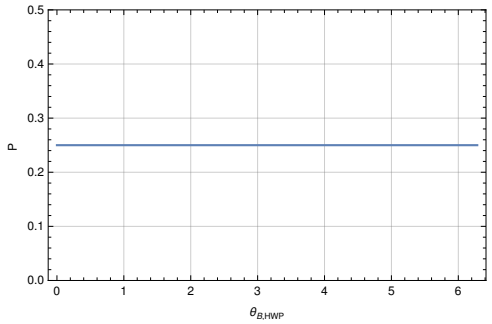

(c) DD

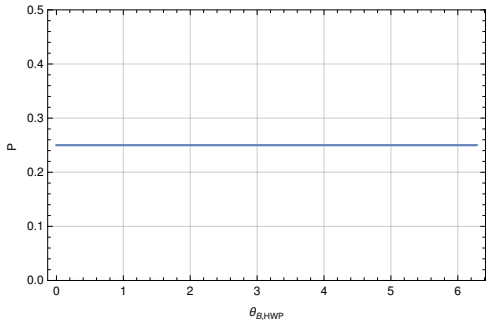

(d) AA

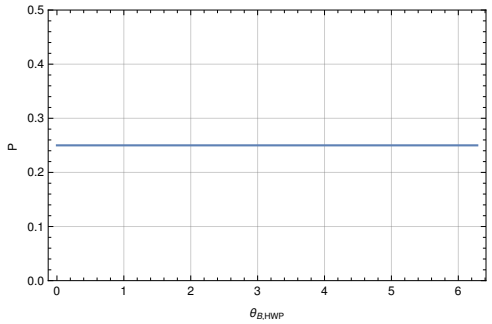

(e) LL

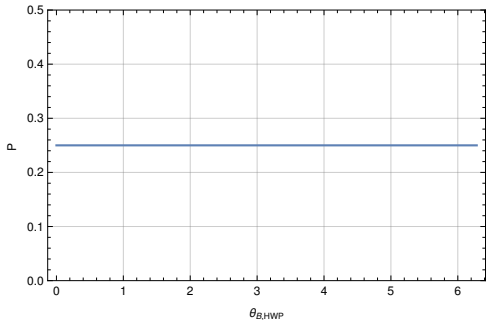

(f) RR

Fig. 3.20: Probabilities of the ensemble $\rho_{mix} = \frac{1}{2}\left(|VV\rangle\langle VV| + |HH\rangle\langle HH|\right)$ in various measurement bases (Table 3.2) plotted over the angle of the half-wave plate θ_{HWP} in the idler arm. In this case there is measurement bases with no fringes. The fidelity of this ensemble using Eq. (2.80) and Eq. (2.81) is $F = 0.5$.

4 Results

4.1 Folded Sandwich

Before placing the nonlinear crystal into the pump beam, the properties of the pump beam after the focusing lens f_p were measured. The result of various measurements at different positions behind the lens is shown in Fig. 4.1. The beam was recorded using a commercial camera and the beam widths were fitted assuming a Gaussian distribution and, in addition, using the knife method. As a result, a beam waist of $w_0 = 24.9\,\mu\text{m}$ was found corresponding to a confocal parameter of $b = 3.26\,\text{mm}$. These parameters are important for estimating the widths of the signal and idler modes leaving the folded sandwich.

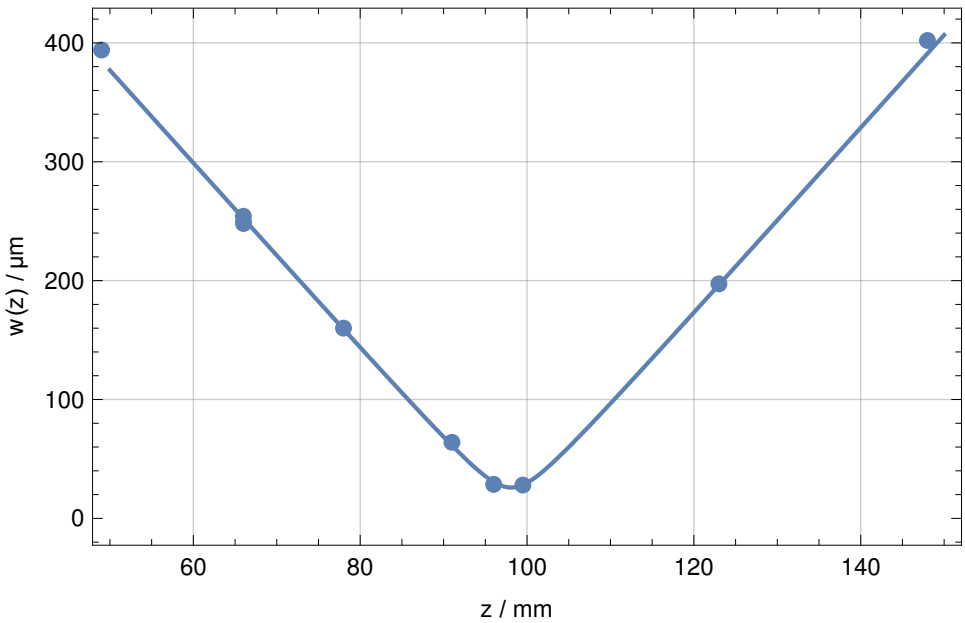

Fig. 4.1: Measurement of the Gaussian beam waist of the pump photons in free air. The beam widths was taken at various positions z behind the plano-convex lens using a commercial camera. The plano-convex lens with focal length $f = 100\,\text{mm}$ focuses the pump light inside the crystal, the optimal position of the waist is the center of the down-conversion crystal. The waist is located at $z = 98.7(6)\,\text{mm}$ with a waist of $w_0 = 24.9(1)\,\mu\text{m}$ and confocal parameter of $b = 3.26(5)\,\text{mm}$.

The polarization rotation is done using a Fresnel rhomb. The polarization was analyzed with the help of the signal mode (Fig.3.1). A polarizer was placed in front of the single mode fiber coupling. The counts on APD1 were recorded while changing the angle of the polarizer's transmission axis. Blocking the second pass of the pump beam using a long-pass filter, absorbing wavelengths smaller than 650 nm, only vertical signal and corresponding idler photons from the first pass are leaving the folded sandwich. As a result, a visibility of $V_{1st} = 86.1(1)\%$ was measured by varying the angle of the transmission axis of the polarizer relative to the signal photons polarization direction. The same measurement should be performed for the idler mode but this is not presented here due to the strong noise in the count rate of APD2. In order to measure only the signal photons emitted in the second pass of the pump photons, the orientation of the pump photons polarization was chosen appropriate. By pumping the first pass of the nonlinear crystal with horizontal polarization, no photon pairs are generated. After double pass through the Fresnel rhomb, the pump photons transform their polarization from horizontal to vertical and a pump photon with vertical polarization is generating signal and idler photons under the specific phase-matching condition. By preparing the pump with horizontal polarization, a visibility of $V_{2nd} = 99.92(1)\%$ was measured for photons emitted in the second pass of the pump photons. This visibility of the first pass is lower than the value measured for the photons emitted in the second pass since the Fresnel rhomb is not perfectly rotating both wavelengths in the double pass from vertical to horizontal. A next step would be to improve this value to get a visibility of almost 100% in both passes. This can be done by finding the optimal position of the rhomb with respect to the two rotation axes. This could be done by an adjustable solid mount for the Fresnel rhomb.
In order to see if the positions of the optical elements are correct and the width of the pump photons is approximately the same as calculated, the width of the pump beam was measured first without the collimating lens f_{si} and in following measurements with the lens placed at different positions behind the dichroic mirror DM1. The calculated width of the pump beam at a distance of 28 cm behind DM1 is about 2000 µm. The experimental value is 1800 µm. This value is near the calculated value and can easily be adjusted to the calculated value by moving the concave mirror in the mm range towards the down-conversion crystal. By placing the lens f_{si} behind DM1, the pump beam is collimated and the right position of the lens can be found relying on the measured beam widths or by finding an optimal coupling to the detectors by varying the position of the lens f_{si}.

4.2 Spontaneous parametric down-conversion

The emission of the down-converted photons was analyzed using the Czerny-Turner spectrograph from Sec. 3.2. With respect to future experiments with the stabilized emission of the quantum dots [Kro12, Mü13], the temperature of the down conversion crystal is set to 131.4 °C. This value corresponds to specific center wavelengths for the signal and idler photons. For finding the right temperature that matches the signal photons with the quantum dot emission the well known emission line of an optical parametric oscillator locked at the cesium frequency standard D1 line at 894.35 nm has been used as a reference for the signal photons. Since in the process of spontaneous parametric down-conversion, momentum and energy conservation must be obtained, the following two conditions hold

$$\omega_p = \omega_s + \omega_i \tag{4.1}$$

$$k_p = k_s + k_i \tag{4.2}$$

Assuming a pump wavelength of 532 nm and a signal wavelength of 894.35 nm leads to an idler wavelength of 1313.1 nm.

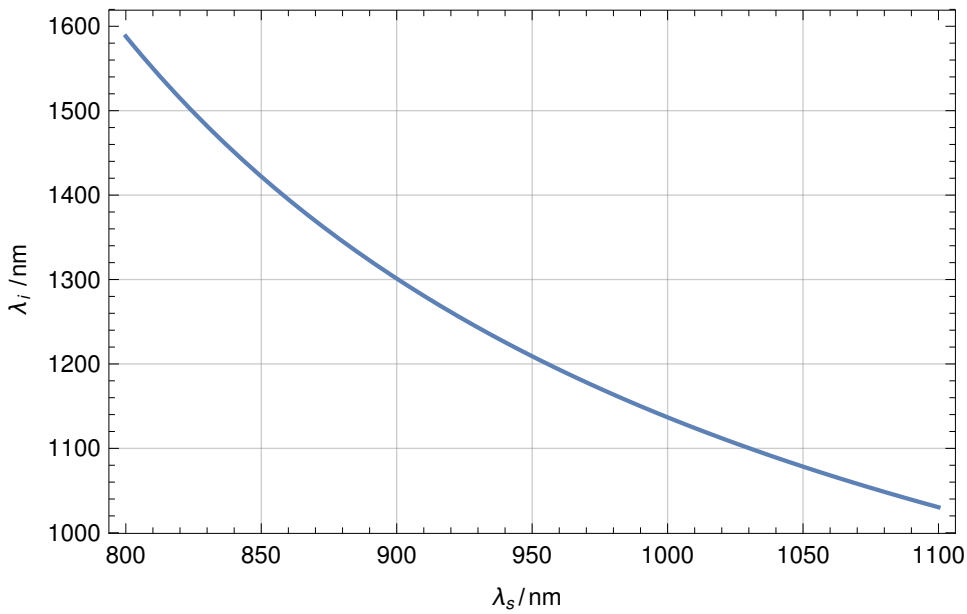

Fig. 4.2: Theoretical curve of available combinations of wavelengths for the signal and idler photons, λ_s and λ_i, under the assumption of $\lambda_p = 532\,\text{nm}$ being the pump photon wavelength. The desired wavelengths are $\lambda_s = 894.35\,\text{nm}$ and $\lambda_i = 1313.1\,\text{nm}$.

The theoretical curve of possible signal and idler pairs with a given pump wavelength of $\lambda_p = 532\,\text{nm}$ using the energy condition expressed in wavelength

$$\lambda_i(\lambda_s) = \left(\frac{1}{\lambda_p} - \frac{1}{\lambda_s}\right)^{-1} \tag{4.3}$$

is shown in Fig. 4.2.
In order to verify the existence of the expected pairs in the signal mode and in the idler mode, the emission was coupled to optical fibers for further characterization. The results of measuring the spectral properties of the down-converted photons are shown in Fig. 4.3.

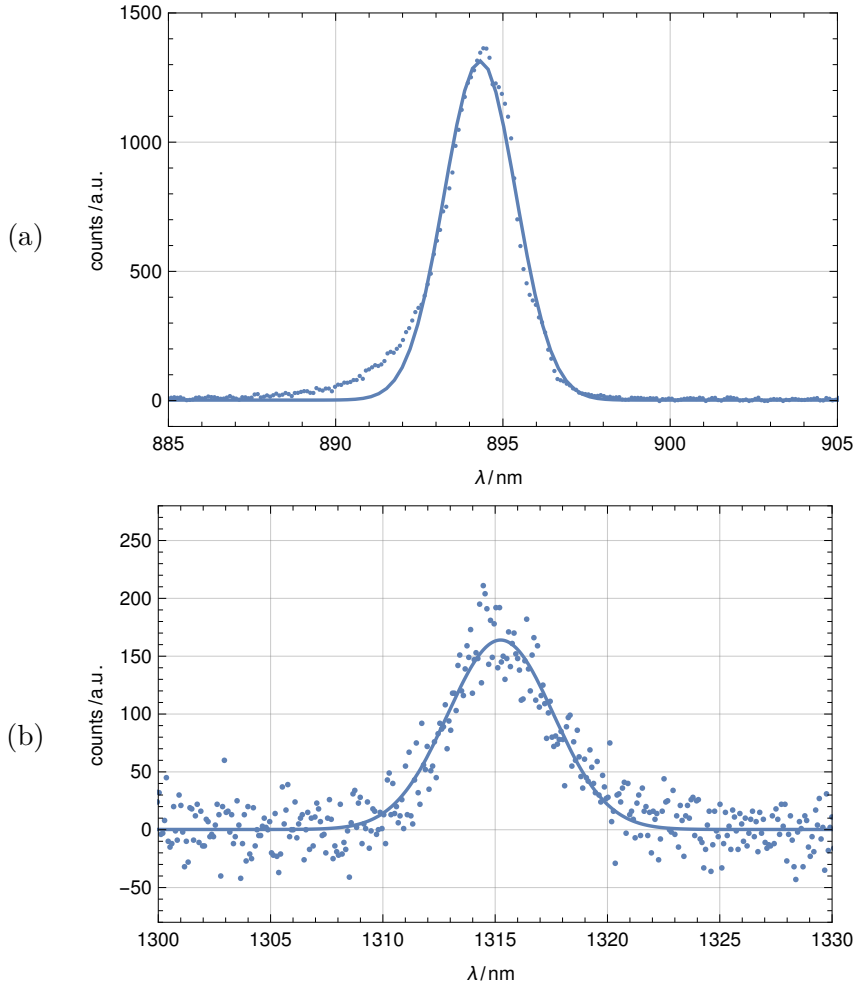

Fig. 4.3: The Spectrum of the signal mode is shown in graph (a). Graph (b) shows the spectrum of the idler mode. The spectra were measured at a down-conversion crystal temperature of 131.4 °C. The material of the down-conversion crystal is MgO:PPLN, the pumped grating structure has a poling period of 7 µm. Both modes were coupled into single-mode fibers. A Gaussian fit gives a full width at half maximum of $\Delta\lambda_{signal} = 2.5\,\mathrm{nm}$ and a center wavelength of $\lambda_{signal} = 894.3\,\mathrm{nm}$ for the signal photons shown in (a). For the idler photons a Gaussian fit gives a full width at half maximum of $\Delta\lambda_{signal} = 5.6\,\mathrm{nm}$ and a center wavelength of $\lambda_{signal} = 1315\,\mathrm{nm}$ shown in (b). The slight offset in order of 2 nm may be due to the change of camera and that there was no reference beam available. In both measurements the grating frequency was $600\,\mathrm{mm}^{-1}$.

The emission was coupled into single mode fibers and sent to the spectrograph. Since the idler wavelength is out of sensitivity for the visible to near infrared camera mounted at the exit slit of the spectrograph, another camera with sensitivity for the infrared range of the idler wavelength was mounted at the exit slit. The change of camera causes a little offset and the spectrograph has to be readjusted to show the correct wavelength on a given camera pixel. Alternatively, a beam with a well known narrow spectrum can be used as a reference.

4.2.1 Spectral Width of Photon Pairs

Assuming a Gaussian profile the spectral bandwidths at full width half maximum are $\Delta\lambda_{signal} = 2.5\,\mathrm{nm}$ for the signal photons and $\Delta\lambda_{idler} = 5.6\,\mathrm{nm}$ for the idler photons, both corresponding to a bandwidth of approximately 6 THz, in good agreement with energy conservation. A lower bandwidth is achievable by a better alignment of the nonlinear crystal. The smallest bandwidth measured for the signal photons was $\Delta\lambda_{signal} = 1.5\,\mathrm{nm}$. In the process of spontaneous parametric down-conversion with monochromatic pumping the single photon bandwidth [Ben10] is proportional to

$$\Delta\omega_{signal} = \Delta\omega_{idler} \propto \frac{2\pi c}{|n_s' - n_i'|}\max\left(\frac{1}{L}, \frac{1}{10b}\right) \tag{4.4}$$

where $|n_s' - n_i'|$ is the group index with

$$n_j' = c\frac{\delta k_j}{\delta\omega} = n_j - \lambda_j\frac{\mathrm{d}n_j}{\mathrm{d}\lambda_j} \tag{4.5}$$

and L is the length of the down-conversion crystal and $b = \xi/L$ is the aggregate confocal length of the modes. The group index can be calculated using the temperature dependent Sellmeier equation of MgO:PPLN [GSGA08].
In the case of strong focusing, i.e. $\xi \geq 10$, the bandwidth is determined by the confocal length $\propto 1/b$. In the case of weak pumping, i.e. $\xi \leq 10$, the bandwidth is smaller, it is inversely proportional to the crystal length $\propto 1/L$.

4.2.2 Tunability

The wavelengths of the generated photon pairs emitted by the quasi-phase matched down-conversion crystal are tunable by changing the temperature of the crystal. The reason for this is, that a change in temperature corresponds to a change in refractive index and therefore to a change in the phase matching condition. The calculated photon bandwidth is shown in Fig. 4.4 together with the measured bandwidth, plotted over the signal photon wavelength. Equation (4.4) holds under the assumption of spontaneous parametric down-conversion sources with small bandwidth, i.e. the bandwidths of the photons must be much smaller than an optical frequency. This assumption is clearly fulfilled since in the setup there is a relative long down-conversion crystal with an expected small bandwidth. The reason for the behavior of (4.4) is that the spectral dependence

of the joint spectral amplitude $\psi(\omega_s, \omega_i)$ arises primarily due to the dispersion of the phase mismatch

$$\Phi = (\Delta k + mK)L \tag{4.6}$$

where m is the order of quasi-phase matching.

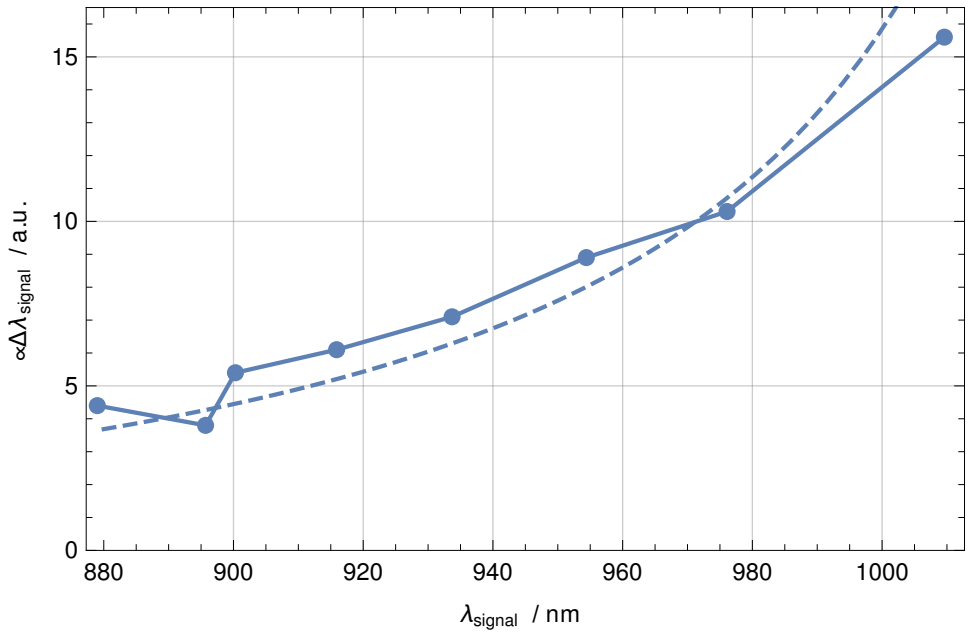

Fig. 4.4: Single photon bandwidth calculated from Eq. (4.4) under the assumption of monochromatic pumping with a Gaussian mode in the weak focusing limit $\xi \leq 10$. The dotted line represents the measured values of the bandwidth, the dashed line represents the calculated bandwidth. The crystal length L is 4 cm, the group index is calculated using the temperature dependent Sellmeier equation of MgO doped periodically poled lithium niobate at a temperature of 131.4 °C. A constant factor of 10^{-8} is multiplied to the bandwidth in order to better fit the measured curve, taking into account the proportionality of Eq. (4.4) and a slight misalignment of the experimental parameters of the setup.

The spectra of the same measurement are shown in Fig. 4.5 for different temperatures, covering a wavelength range for the signal photons of more than one hundred nanometers. During the measurement the coupling of the signal mode had to be readjusted, since the change in temperature can lead to a change in position of the crystal.

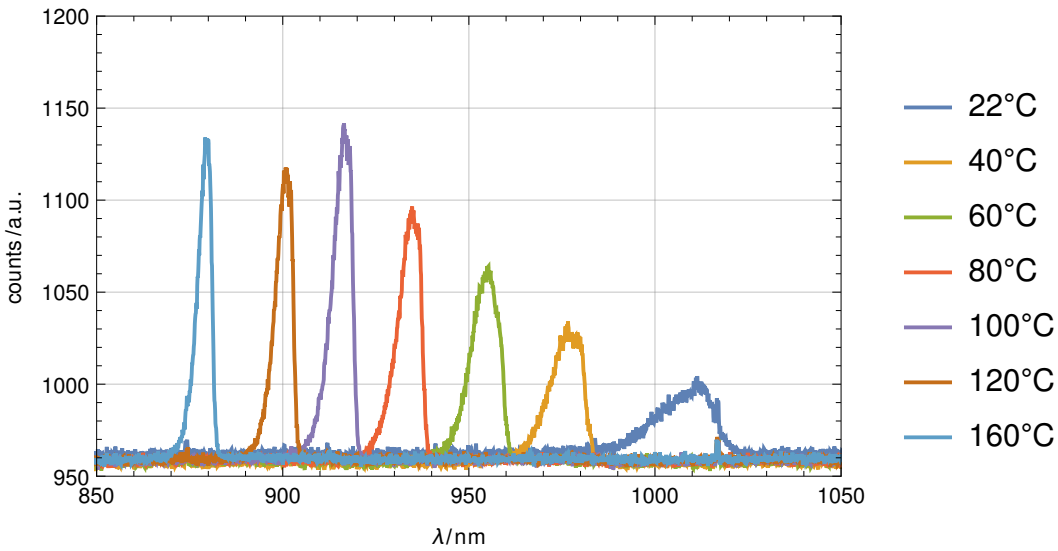

Fig. 4.5: Spectra of the signal mode measured at several crystal temperatures from 22 °C to 160 °C using a MgO:PPLN down-conversion crystal with poling period 7 µm. The temperature dependence of the signal photons center wavelength $\lambda_{signal}(T)$ is roughly 1 nm/°C. The reason for the smaller amount of counts with growing wavelength is the detection efficiency of the camera. For the measured wavelength range it is a linear function of wavelength. The two peaks at 120°C and 160°C are new measurements after a re-alignment of the crystal position.

4.2.3 Brightness

Another important characteristic is the number of generated pairs. According to the detailed analysis of spontaneous parametric down-conversion with collinear Gaussian beams by Bennink [Ben10], there is a theoretical upper bound for the signal probability P_s, that is the probability that a signal photon is emitted into the signal mode

$$P_s \leq \frac{32\pi^4 \hbar c \epsilon n_s n_i}{3\epsilon_0 n_p |n_s' - n_i'|} \left(\frac{\chi_{eff}^{(2)}}{\lambda_s \lambda_i} \right)^2 N_p \tag{4.7}$$

For the experimental setup, this yields an upper bound of

$$P_s \leq 7 \cdot 10^2 \, \frac{\text{Mcps}}{\text{mW}} \tag{4.8}$$

signal photons per second. This value is calculated assuming 1 mW of pump power, using the following parameters

$$\begin{aligned}
\epsilon &= 1 \quad \text{(efficiency factor)} \\
n_p &= 2.26 \quad \text{(from [GSGA08] at 532 nm and 131.4°C)} \\
n_s &= 2.19 \quad \text{(from [GSGA08] at 894.35 nm and 131.4°C)} \\
n_i &= 2.17 \quad \text{(from [GSGA08] at 1313.1 nm and 131.4°C)} \\
|n_s' - n_i'| &= 0.02 \quad \text{(group index, see Eq. (4.5))} \\
\chi_{eff}^{(2)} &= d_{QPM} = 15.9\,\text{pm/V} \quad \text{(effective nonlinear coefficient for MgO:PPLN [SKK+97]} \\
\lambda_s &= 894.35\,\text{nm} \\
\lambda_i &= 1313.1\,\text{nm} \\
N_p &= 2.68 \cdot 10^{15}\, s^{-1} \quad \text{(calculated number of pump photons per second per mW)}
\end{aligned}$$

Taking the detector efficiency into account, an experimentally achievable measurement value of the signal count rate per second and per mW pump power may be at the order of 270 Mcps. This theoretical value is not in good agreement with the measured value of 20 Mcps, even though no corrections for loss in the optical elements were included in the calculation. The calculated value is an upper bound for optimal focusing parameters. By estimating our actual focusing parameters as $w_s = 24.9\,\mu\text{m}$, $w_s = 31.5\,\mu\text{m}$ and $w_i = 38.2\,\mu\text{m}$ the corrected probability is [Ben10]

$$P_s \approx \frac{64\pi^3 \hbar c \epsilon n_s n_i}{\epsilon_0 n_p |n_s' - n_i'|} \left(\frac{\chi_{eff}^{(2)}}{\lambda_s \lambda_i} \right)^2 \frac{\arctan\left(\frac{B_s}{A_s}\xi_s\right)}{A_s B_s} N_p \tag{4.9}$$

This gives a corrected value of

$$P_s \approx 61 \, \frac{\text{Mcps}}{\text{mW}} \tag{4.10}$$

per mW pump power, after taking the detector efficiency into account. The quantities A_s and B_s are depending on the focus of the signal and idler relative to the pump. According to Eq. 2.18, the focal parameter is defined as $\xi_s = L/(k_s w_s^2)$. Since the maximum measured value was 20 Mcps per mW pump power, the count rate could still be improved.

4.3 Photon Pair generation

In the quantum mechanical description of parametric down-conversion a single pump photon ω_p splits spontaneously into two photons ω_s and ω_i. Burnham and Weinberg [BW70] have verified this description by observing coincidences between photons emitted by an ammonium dihydrogen phosphate crystal pumped by a 325 nm pump laser. Assuming simultaneity in emission of a signal and idler pair, a click on the heralding detector APD1 should correspond to a click on detector APD2. Since there is much noise in count rate on detector APD2, it is run in a triggered mode. A signal photon traveling along a relative short optical fiber coupled to the detector APD1, causes a pulse when hitting the detector. The pulse is then sent to APD2 using a commercial BNC cable where it is opening the gate for a short time window τ_{gate}. In order to find the right time delay for opening the gate, a sufficiently long optical fiber for the idler mode and a delay box on the heralding BNC line between APD1 and APD2 is needed for adjusting the time delay between the heralding photon and the opening of the gate at APD2. The duration of the gate window is an important parameter for the reduction of noise leading to a high detection efficiency. In addition, the dead time and the detection efficiency is adjustable.

In order to record the measurement, the output of APD1 was sent on one input port of a time correlator while the output of APD2 was sent on the other port. The result of the comparison of both inputs is shown in Fig. 4.6. A click on APD1 is used as a start count, a click on APD2 is stopping the measurement and the time delay between these both events is stored. The three curves belong to different time delays, all being in a time interval of 4 ns. The duration of the gate window was set to 5 ns, which can be seen directly in the plotted curves. The curve corresponding to a delay of 80 ns is in the range where the setup is adjusted to measure coincidence counts between the photon pairs. As will be shown later, the width of this curve is not the width between the creation times of signal and idler in the down-conversion process. The width of the curve is broadened due to the detection process, i.e. the timing jitter. In the curve corresponding to 78 ns no photon pairs were measured in coincidence. The height of the curve is mainly caused by false coincidences or background noise of the involved detectors.

In Fig. 4.7 a gate duration of 20 ns was chosen, leading to a higher noise in the detection process. By varying the time delay on the delay box it was possible to directly observe that the signal idler coincidence peak is staying at the same time delay while the 20 ns broad gate window is moving according to the setting of the time delay. A fit of the coincidence peak gives a full width at half maximum of $\Delta t_{exp} = 680$ ps. The jitter of the two detectors is given according to the manufacturer to about 500 ps. Taking

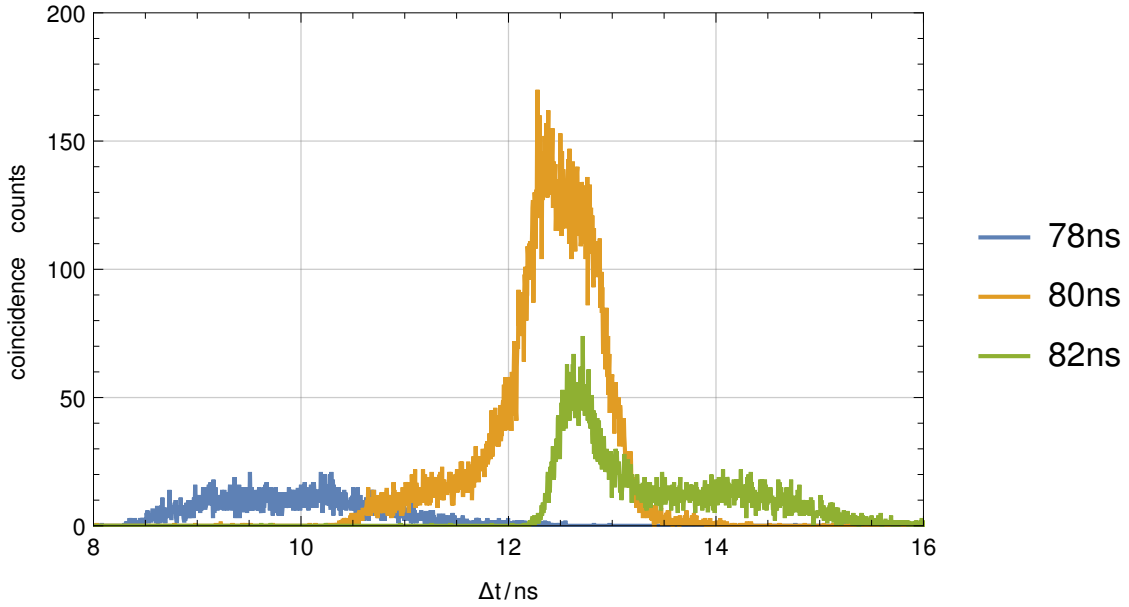

Fig. 4.6: Measured signal and idler coincidences using a 5 ns gate width and different adjusted temporal delays of 78 ns, 80 ns and 82 ns between the signal and idler detections (Fig. 3.17). Only for a certain time delay in the range of 80 ns the coincidence rate is much greater than the accidental rate. The time of acquisition was 20 s.

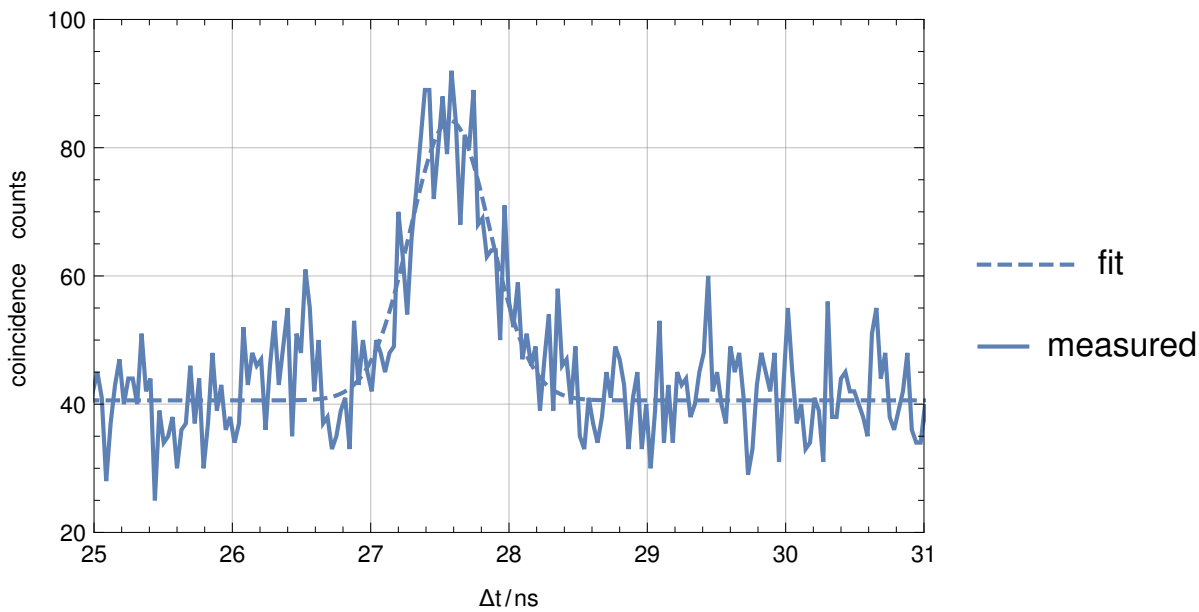

Fig. 4.7: Measured signal and idler coincidences using 20 ns gate width, FWHM of 680 ps was taken out of a Gaussian fit. The time of acquisition was 20 s.

into account that one is measuring in coincidence, which means that one measures the superposed jitter of both detectors, a value of $\Delta t_{theo} = \sqrt{2} \times 500\,\text{ps} = 707\,\text{ps}$ can be calculated in good agreement with the experimentally revealed value.
Using highly efficient fiber coupled superconducting single photon detectors for the signal and idler mode, along with the feature of low noise and low false detections, it was possible to measure coincidences without the need for triggering the gate of one of the detectors. The measurement result is plotted in Fig. 4.8 together with a Gaussian fit yielding a full width at half maximum of 71 ps. The jitter of these single photon detectors is given to be $\Delta t = 50\,\text{ps}$. The resulting width of detection involving to detectors is therefore $\Delta t_{theo} = 71\,\text{ps}$, which is in good agreement with the measured value of $\Delta t_{exp} = 71\,\text{ps}$. With the avalanche photo diodes such a direct coincidence measurement, i.e. without triggering one of the detectors, would only result in noise. The SSPDs were provided by the Reitzenstein group at TU Berlin.

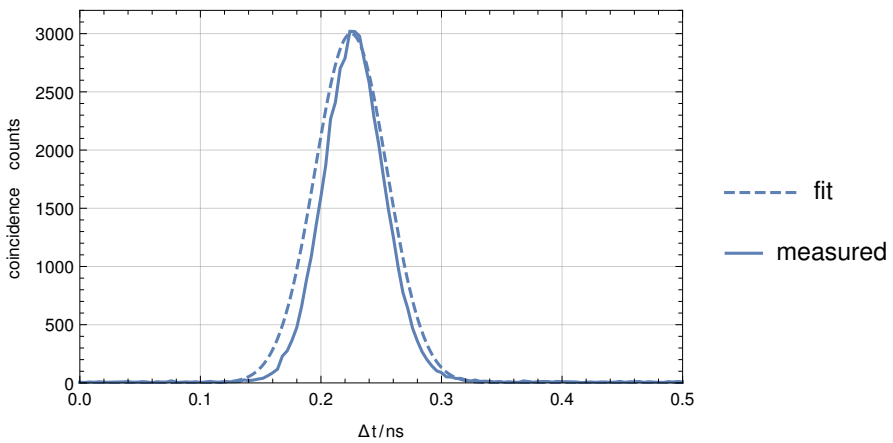

Fig. 4.8: Signal and idler coincidence counts, measured with superconducting single photon detectors (SSPDs), FWHM 71 ps. The time of acquisition was 30 s.

4.4 Single mode coupling

For building a high brightness photon pair source, an efficient single mode coupling is essential. Important for an efficient single mode coupling is the gaussian shape of the spatial emission pattern. The spatial emission pattern of the signal mode is shown in Fig. 4.9. The signal mode has a Gaussian shape before it gets coupled to the optical fibers.

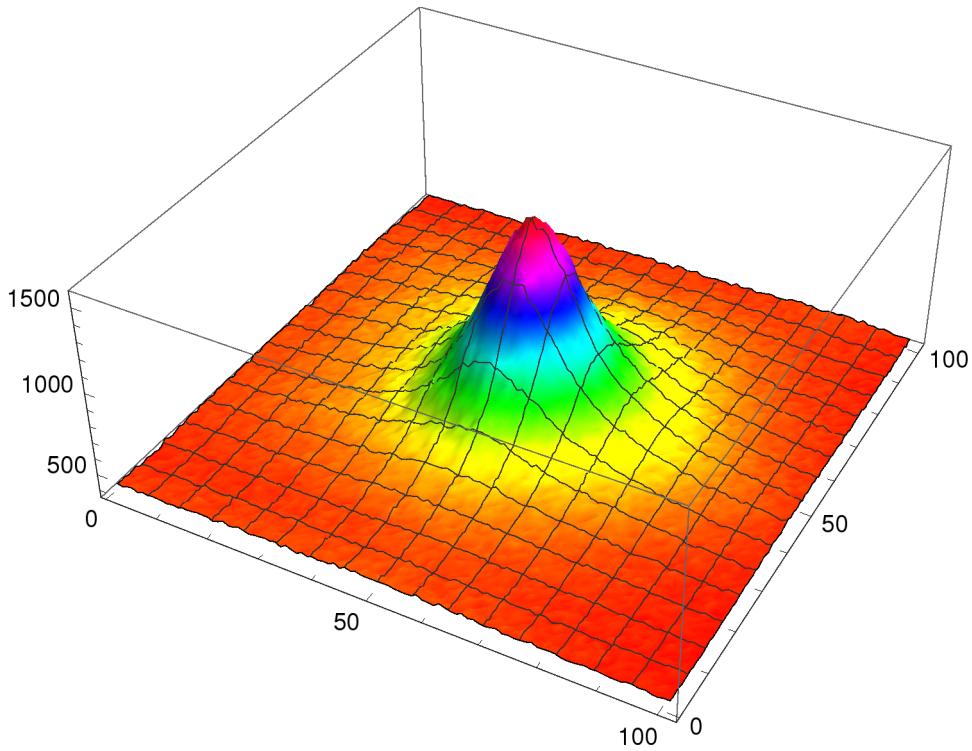

Fig. 4.9: Signal photons measured using a CCD camera positioned 90 cm behind the collimating lens f_{si} (Fig. 3.2). During the measurement, the pump beam was blocked using two long-pass filters.

The beam widths at the position of the collimation optics, coupling the light into the respective single mode fiber, can be estimated using the calculated values from Sec. 3.3. The expected coupling efficiency can be estimated using the following equation [Pas10]

$$\eta = \frac{4w_0^2 w_{fiber}^2}{(w_0^2 + w_{fiber}^2)^2} \tag{4.11}$$

Using the calculated values for the beam waists (Fig. 3.14) and the mode field diameter leads to an efficiency of about 99.6% for the idler mode and an efficiency of about 95.2% for the signal mode. In order to couple the emission more efficiently, one could set up a beam transformation, using two lenses with appropriate focal lengths positioned in the signal arm. This leads to a calculated efficiency of 99.9% for the coupling of the

signal mode. These values are upper bounds for the experimentally achievable efficiency assuming perfect mode matching in all other degrees of freedom.

4.5 Entanglement detection

For the detection of entanglement the gated coincidence setup was used (see Fig. 3.17). This setup allows to perform joint measurments of the signal and idler photons of a photon pair. By changing the measurement bases in the respective signal and idler arm the correlations of the two-photon state can be measured. The actual measurements shown in Fig. 4.10 were taken varying the settings of the polarizer, the half-wave plate and the quarter-wave plate

basis	signal arm		idler arm	
	θ_A	θ_{QWP}	θ_B	θ_{QWP}
VV	0	-	0	-
HV	90	-	0	-
DV	45	-	0	-
AV	315	-	0	-
RV	-22.5	-45	0	-45
LV	22.5	45	0	45

Table 4.1: Orientations of the optical elements in the measurement shown in Fig. 4.10.

A common source of noise in optical measurements is a constant background on the detectors. In the setup where the telecom APD2 is triggered by the signal APD1 there was nearly no background in coincidence counts when measuring using a gate time window of $\tau_{gate} = 2\,\text{ns}$.
Another common source of of noise is accidental coincidences due to uncorrelated photons hitting the telecom detector during an open gate window τ. The accidental coincidence rate per second can be calculated as

$$N_{cc}^{acc} = \frac{R_1 \cdot R_2 \cdot \tau_{gate}}{T_{acq}} \tag{4.12}$$

where $R_{1,2}$ are the singles count rates per second of detectors APD1 and APD2, τ is the gate window at APD1 in which a photon will be registered as coincident with a photon detected at APD2 and T_{acq} is the time of acquisition. For example, during the measurement in the VV basis, the count rate on APD1 was $R_1 = 0.4\,\text{Mcps}$, the count rate on APD2 was $R_2 = 10\,\text{kcps}$ and the coincidence rate was $R_c = 9.5\,\text{kcps}$. This leads to a value of $N_{cc}^{acc} = 0.4\,\text{cps}$. This source of noise is present in the coincidence circuit, however, it stays well below the statistical error of the coincidence rate measurements.

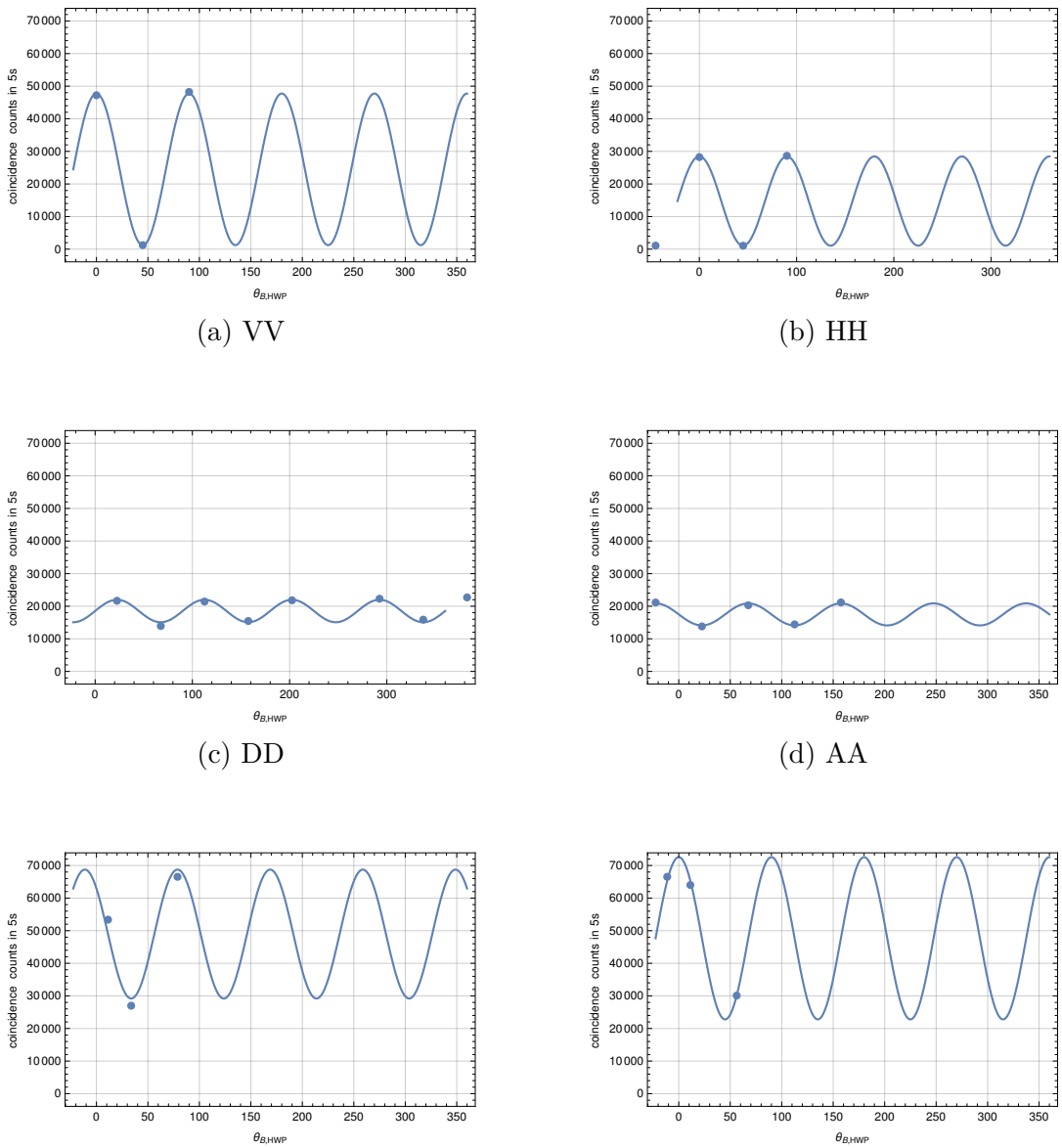

(a) VV (b) HH

(c) DD (d) AA

(e) LL (f) RR

Fig. 4.10: Measuring the correlations of the photon pairs produced by the folded sandwich in various different measurement bases (Table 3.2). In addition to the polarizers A and B, quarter- and half-wave plates were introduced in both arms. The plotted curves were obtained as a best fit using the visibility as the fitting parameter. During the whole measurement several YVO4 crystals with a total length of $L_{YVO4} \approx 10\,\text{cm}$ were introduced for phase compensation.

The presence of entanglement can be detected using various measures. As can be seen in the previous section, the generated state is highly correlated in the H/V- basis and less correlated in all other measured bases. These correlations are unique to entangled quantum systems. To discriminate between an entangled and a separable state the Bell-

state fidelity F and the entanglement witness W can be calculated. Using Eq. (2.80) and Eq. (2.81) [WGP+07] for the fitted measurement results shown in Fig. 4.10, the calculated values for the Bell state fidelity are

$$F_{\phi^+} = 0.385(2) \tag{4.13}$$
$$F_{\phi^-} = 0.586(2) \tag{4.14}$$

The value for F_{ϕ^-} shows that the generated state is an entangled state, since all states with a Bell-state fidelity of $F > 50\%$ are entangled. The actual joint-probabilities were not always measured directly but taken out of the best fit for the visibilities. For the entanglement witness W the calculated values using Eq. (2.95) and Eq. (2.96) are

$$W_{\phi+} = +0.115(3) \tag{4.15}$$
$$W_{\phi-} = -0.086(3) \tag{4.16}$$

and therefore also shows entanglement since the entanglement witness W is negative. One can compare the values for F and W with Eq. (2.99)

$$W_{\phi^-} = \frac{1}{2} - F_{\phi^-} \tag{4.17}$$
$$= -0.086(2) \tag{4.18}$$

This value corresponds to the calculated value from Eq. (4.16). In general both values should not exactly correspond to each other. The reason that the fidelity leads exactly to the witness is that the values N_{ij} were taken out of the fitted curves. By directly measuring both observables, the results will in general be independent.

4.6 Discussion

The results in Sec. 4.5 are indicating the presence of entanglement in the generated state. However, the overlap with an ideal Bell state is still very low. In a measurement with the compensation crystal rotated about 90°, the result was that in the diagonal basis no more correlations were present. Regarding a mixed Werner state, the result of the measurements is not consistent with some distinct value of p leading to the same amount of decoherence in all bases. It is to be noted that there is less coincidences in the horizontal basis than in the vertical, although the singles counts of the horizontal and vertical photons were the same. Since rotating the compensation crystal erased the correlations in the diagonal basis, a way to achieve a higher overlap with the Bell state is to find the optimal length of the compensation crystal and to tune the temperature of the crystal oven. This is a new setup build up from scratch and these measurements are one of the first measurements with the compensation crystals in the optical path. Entanglement was detected for a Bell state $|\phi^-\rangle$.

5 Outlook

The folded sandwich was built up and the properties of the down-converted photons were analyzed. A measurement circuit was built to assess the correlations between the generated photon pairs produced either in the first or the second pass of the nonlinear crystal. The main result is that the produced photon pairs were detected in pairs and show entanglement in their polarization degree of freedom.
The calculated values for the detection of entanglement are not yet optimal and it needs further effort to improve those values. This can be done by an improved focusing of the pump photons in order to produce indistinguishable photons in both passes. The orientation of the Fresnel rhomb can be improved to get only orthogonal pairs of photons. An important component is the compensation crystal and the crystal oven. Changing the temperature of the crystal oven will adjust one of two ideal Bell states.
In future experiments it is planned to demonstrate the teleportation of flying qubits emitted from semiconductor quantum dots. The quantum dots are stabilized to the cesium D1 line at 894.35 nm. In order to teleport the state of a quantum dot photon to the telecom band, the source of entangled photon pairs needs to operate at non-degenerate wavelengths.
The first step towards the entanglement swapping is done, more effort has to be done in future experiments in order to adjust a phase-stable source of two-color polarization-entangled photon pairs. This work is embedded in a larger project with the goal to perform entanglement swapping.

Bibliography

[ABDP62] J. A. Armstrong, N. Bloembergen, J. Ducuing, and P. S. Pershan, *Interactions between Light Waves in a Nonlinear Dielectric*, Physical Review **127** (1962), no. 6, 1918–1939.

[ADR82] Alain Aspect, Jean Dalibard, and Gérard Roger, *Experimental Test of Bell's Inequalities Using Time- Varying Analyzers*, Physical Review Letters **49** (1982), no. 25, 1804–1807.

[AGR81] Alain Aspect, Philippe Grangier, and Gérard Roger, *Experimental Tests of Realistic Local Theories via Bell's Theorem*, Physical Review Letters **47** (1981), no. 7, 460–463.

[AJK] J. Altepeter, E. Jeffrey, and P. Kwiat, *Photonic State Tomography.*

[BA57] D. Bohm and Y. Aharonov, *Discussion of Experimental Proof for the Paradox of Einstein, Rosen and Podolsky*, Physical Review Letters **108** (1957), no. 4, 1070–1076.

[BDCZ98] H.-J. Briegel, W. Dür, J. I. Cirac, and P. Zoller, *Quantum Repeaters: The Role of Imperfect Local Operations in Quantum Communication*, Physical Review Letters **81** (1998), no. 26, 5932–5935.

[BDMDN+03] M. Barbieri, F. De Martini, G. Di Nepi, P. Mataloni, G. M. D'Ariano, and C. Macchiavello, *Detection of Entanglement with Polarized Photons: Experimental Realization of an Entanglement Witness*, Physical Review Letters **91** (2003), no. 22, 227901.

[Bel64] John S. Bell, *On the Einstein Podolsky Rosen Paradox*, Physics **Vol. 1** (1964), no. 3.

[Ben10] Ryan S. Bennink, *Optimal collinear Gaussian beams for spontaneous parametric down-conversion*, Physical Review A **81** (2010), no. 5, 053805.

[BK68] G. D. Boyd and D. A. Kleinman, *Parametric Interaction of Focused Gaussian Light Beams*, Journal of Applied Physics **39** (1968), no. 8, 3597–3639.

[Boy08] Robert W. Boyd, *Nonlinear Optics*, 3 ed., Academic Press, March 2008.

[BPM+97] Dik Bouwmeester, Jian-Wei Pan, Klaus Mattle, Manfred Eibl, Harald Weinfurter, and Anton Zeilinger, *Experimental quantum teleportation*, Nature **390** (1997), no. 6660, 575–579 (en).

[BW70] David C. Burnham and Donald L. Weinberg, *Observation of Simultaneity in Parametric Production of Optical Photon Pairs*, Physical Review Letters **25** (1970), no. 2, 84–87.

[BW99] Max Born and Emil Wolf, *Principles of Optics: Electromagnetic Theory of Propagation, Interference and Diffraction of Light*, 7 ed., 1999.

[CHSH69] J. F. Clauser, M. A. Horne, A. Shimony, and Richard A. Holt, *Proposed Experiment to Test Local Hidden-Variable Theories*, Physical Review Letters **23** (1969), no. 15, 880–884.

[Cla76] John F. Clauser, *Experimental Investigation of a Polarization Correlation Anomaly*, Physical Review Letters **36** (1976), no. 21, 1223–1226.

[CS78] J. F. Clauser and A. Shimony, *Bell's theorem. Experimental tests and implications*, Reports on Progress in Physics **41** (1978), no. 12, 1881 (en).

[EPR35] A. Einstein, B. Podolsky, and N. Rosen, *Can Quantum-Mechanical Description of Physical Reality Be Considered Complete?*, Physical Review **47** (1935), no. 10, 777–780.

[FB08] Marco Fiorentino and Raymond G. Beausoleil, *Compact sources of polarization-entangled photons*, Optics Express **16** (2008), no. 24, 20149–20156.

[FC72] Stuart J. Freedman and John F. Clauser, *Experimental Test of Local Hidden-Variable Theories*, Physical Review Letters **28** (1972), no. 14, 938–941.

[FHP+07] Alessandro Fedrizzi, Thomas Herbst, Andreas Poppe, Thomas Jennewein, and Anton Zeilinger, *A wavelength-tunable fiber-coupled source of narrowband entangled photons*, Optics Express **15** (2007), no. 23, 15377–15386.

[foc14] *Foctek Photonics - YVO4*, `http://www.foctek.net/products/YVO4.htm`, August 2014.

[FT76] Edward S. Fry and Randall C. Thompson, *Experimental Test of Local Hidden-Variable Theories*, Physical Review Letters **37** (1976), no. 8, 465–468.

[GFT+12] W. B. Gao, P. Fallahi, E. Togan, J. Miguel-Sanchez, and A. Imamoglu, *Observation of entanglement between a quantum dot spin and a single photon*, Nature **491** (2012), no. 7424, 426–430 (en).

[GSGA08] O. Gayer, Z. Sacks, E. Galun, and A. Arie, *Temperature and wavelength dependent refractive index equations for MgO-doped congruent and stoichiometric LiNbO3*, Applied Physics B **91** (2008), no. 2, 343–348 (en).

[GT09] Otfried Gühne and Géza Tóth, *Entanglement detection*, Physics Reports **474** (2009), no. 1–6, 1–75.

[HHH96] Michał Horodecki, Paweł Horodecki, and Ryszard Horodecki, *Separability of mixed states: necessary and sufficient conditions*, Physics Letters A **223** (1996), no. 1–2, 1–8.

[JKMW01] Daniel F. V. James, Paul G. Kwiat, William J. Munro, and Andrew G. White, *On the Measurement of Qubits*, Physical Review A **64** (2001), no. 5, arXiv: quant-ph/0103121.

[JRY+10] Xian-Min Jin, Ji-Gang Ren, Bin Yang, Zhen-Huan Yi, Fei Zhou, Xiao-Fan Xu, Shao-Kai Wang, Dong Yang, Yuan-Feng Hu, Shuo Jiang, Tao Yang, Hao Yin, Kai Chen, Cheng-Zhi Peng, and Jian-Wei Pan, *Experimental free-space quantum teleportation*, Nature Photonics **4** (2010), no. 6, 376–381 (en).

[KMW+95] Paul G. Kwiat, Klaus Mattle, Harald Weinfurter, Anton Zeilinger, Alexander V. Sergienko, and Yanhua Shih, *New High-Intensity Source of Polarization-Entangled Photon Pairs*, Physical Review Letters **75** (1995), no. 24, 4337–4341.

[Kro12] Tim Kroh, *Charakterisierung von Quantenpunkt-Einzelphotonen für Quantenrepeater-Anwendungen*, Masterarbeit, Humboldt-Universität zu Berlin, 2012.

[Kwi99] Paul Kwiat, *Ultrabright source of polarization-entangled photons*, Physical Review A **60** (1999), no. 2, R773–R776.

[LKCH00] M. Lewenstein, B. Kraus, J. I. Cirac, and P. Horodecki, *Optimization of entanglement witnesses*, Physical Review A **62** (2000), no. 5, 052310.

[LT05] Daniel Ljunggren and Maria Tengner, *Optimal focusing for maximal collection of entangled narrow-band photon pairs into single-mode fibers*, Physical Review A **72** (2005), no. 6, 062301.

[LTMP06] Daniel Ljunggren, Maria Tengner, Philip Marsden, and Matthew Pelton, *Theory and experiment of entanglement in a quasi-phase-matched two-crystal source*, Physical Review A **73** (2006), no. 3, 032326.

[Mes08] Dieter Meschede, *Optik, Licht und Laser*, Vieweg + Teubner in GWV Fachverlage, Wiesbaden, 2008 (German).

[Mü13] Chris Müller, *Automation of an optical setup for investigation of quantum dots*, Bachelorarbeit, Humboldt-Universität zu Berlin, 2013.

[NC10] Michael A. Nielsen and Isaac L. Chuang, *Quantum Computation and Quantum Information: 10th Anniversary Edition*, Cambridge University Press, December 2010 (en).

[OFV09] Jeremy L. O'Brien, Akira Furusawa, and Jelena Vučković, *Photonic quantum technologies*, Nature Photonics **3** (2009), no. 12, 687–695.

[Ou07] Zhe-Yu Jeff Ou, *Multi-Photon Quantum Interference*, Springer Science & Business Media, June 2007 (en).

[Pas10] Rüdiger Paschotta, *Field Guide to Optical Fiber Technology*, SPIE, 1000 20th Street, Bellingham, WA 98227-0010 USA, January 2010 (en).

[PBWZ98] Jian-Wei Pan, Dik Bouwmeester, Harald Weinfurter, and Anton Zeilinger, *Experimental Entanglement Swapping: Entangling Photons That Never Interacted*, Physical Review Letters **80** (1998), no. 18, 3891–3894.

[Per96] Asher Peres, *Separability Criterion for Density Matrices*, Physical Review Letters **77** (1996), no. 8, 1413–1415, arXiv: quant-ph/9604005.

[Ram11] Sven Ramelow, *Experiments on quantum frequency conversion of photons*, Dissertation, Universität Wien, 2011.

[RMG+13] Sven Ramelow, Alexandra Mech, Marissa Giustina, Simon Gröblacher, Witlef Wieczorek, Jörn Beyer, Adriana Lita, Brice Calkins, Thomas Gerrits, Sae Woo Nam, Anton Zeilinger, and Rupert Ursin, *Highly efficient heralding of entangled single photons*, Optics Express **21** (2013), no. 6, 6707–6717.

[SKK+97] Ichiro Shoji, Takashi Kondo, Ayako Kitamoto, Masayuki Shirane, and Ryoichi Ito, *Absolute scale of second-order nonlinear-optical coefficients*, Journal of the Optical Society of America B **14** (1997), no. 9, 2268–2294.

[SRJ+13] Fabian Steinlechner, Sven Ramelow, Marc Jofre, Marta Gilaberte, Thomas Jennewein, Juan. P. Torres, Morgan W. Mitchell, and Valerio Pruneri, *Phase-stable source of polarization-entangled photons in a linear double-pass configuration*, Optics Express **21** (2013), no. 10, 11943–11951.

[ST14] Yoichi Sato and Takunori Taira, *Highly accurate interferometric evaluation of thermal expansion and dn/dT of optical materials*, Optical Materials Express **4** (2014), no. 5, 876–888.

[Tak01] Shigeki Takeuchi, *Beamlike twin-photon generation by use of type II parametric downconversion*, Optics Letters **26** (2001), no. 11, 843–845.

[Ter02] Barbara M. Terhal, *Detecting quantum entanglement*, Theoretical Computer Science **287** (2002), no. 1, 313–335.

[TW08] P. Trojek and H. Weinfurter, *Collinear source of polarization-entangled photon pairs at nondegenerate wavelengths*, Applied Physics Letters **92** (2008), no. 21, 211103.

[Uhl76] A. Uhlmann, *The "transition probability" in the state space of a $*$-algebra*, Reports on Mathematical Physics **9** (1976), no. 2, 273–279.

[UTSM+07] R. Ursin, F. Tiefenbacher, T. Schmitt-Manderbach, H. Weier, T. Scheidl, M. Lindenthal, B. Blauensteiner, T. Jennewein, J. Perdigues, P. Trojek, B. Ömer, M. Fürst, M. Meyenburg, J. Rarity, Z. Sodnik, C. Barbieri, H. Weinfurter, and A. Zeilinger, *Entanglement-based quantum communication over 144 km*, Nature Physics **3** (2007), no. 7, 481–486 (en).

[WGP+07] Andrew G. White, Alexei Gilchrist, Geoffrey J. Pryde, Jeremy L. O'Brien, Michael J. Bremner, and Nathan K. Langford, *Measuring two-qubit gates*, Journal of the Optical Society of America B **24** (2007), no. 2, 172–183.

[Wor76] S. L. Woronowicz, *Positive maps of low dimensional matrix algebras*, Reports on Mathematical Physics **10** (1976), no. 2, 165–183.

[WZ82] W. K. Wootters and W. H. Zurek, *A single quantum cannot be cloned*, Nature **299** (1982), no. 5886, 802–803 (en).

[ZLC+10] David E. Zelmon, Julie J. Lee, Kelly M. Currin, Jessica M. Northridge, and Dan Perlov, *Revisiting the optical properties of Nd doped yttrium orthovanadate*, Applied Optics **49** (2010), no. 4, 644–647.

A Refractive indexes / Sellmeier equations

A.1 Refractive index of BK7 [Mes08]

$$n^2(\lambda) - 1 = \frac{B_1\lambda^2}{\lambda^2 - C_1} + \frac{B_2\lambda^2}{\lambda^2 - C_2} + \frac{B_3\lambda^2}{\lambda^2 - C_3} \tag{A.1}$$

Parameters	BK7
B_1	1.0396
B_2	0.231 79
B_3	1.0105
C_1	0.0060
C_2	0.0200
C_3	103.56

Table A.1: Sellmeier parameters for BK7.

A.2 Refractive indexes of yttrium ortho vanadate (YVO4)

A.2.1 Foctek Photonics [foc14]

$$n^2(\lambda) = A + \frac{B}{\lambda^2 - C} - D\lambda^2 \tag{A.2}$$

Parameters	YVO4 (Manufacturer)	
	n_e	n_o
A	4.5909	3.778 34
B	0.110 534	0.069 736
C	0.048 13	0.047 24
D	0.012 267 6	0.010 813 3

Table A.2: Parameters in sellmeier equation for YVO4.

A.2.2 Sato [ST14]

$$n^2(\lambda) = A + \frac{B}{\lambda^2 - C} - D\lambda^2 \tag{A.3}$$

Parameters	YVO4 (Sato)	
	n_e	n_o
A	4.631	3.793
B	0.097 36	0.064 37
C	0.064 66	0.056 41
D	0.021 89	0.014 28

Table A.3: Parameters in sellmeier equation for YVO4.

A.2.3 Zelmon [ZLC+10]

$$n^2(\lambda) = A + \frac{B\lambda^2}{\lambda^2 - C} + \frac{D\lambda^2}{\lambda^2 - E} \tag{A.4}$$

Parameters	0.5% Nd:YVO4 (Zelmon)	
	n_e	n_o
A	2.7582	2.3409
B	1.853	1.4402
C	0.056 986	0.048 25
D	3.0749	1.8698
E	195.06	171.27

Table A.4: Parameters in sellmeier equation for 0.5% Nd:YVO4.

A.3 Refractive indexes of 5 % MgO doped, periodically poled congruent lithium niobate (MgO:PPLN) [GSGA08]

In the paper by Gayer et al. [GSGA08] the sellmeier equation is assumed to be dependent on wavelength and temperature, it is assumed to have the following form

$$n_e^2 = a_1 + b_1 f + \frac{a_2 + b_2 f}{\lambda^2 - (a_3 + b_3 f)^2} + \frac{a_4 + b_4 f}{\lambda^2 - a_5^2} - a_6 \lambda^2 \tag{A.5}$$

where the parameters a_3 and a_5 account for poles in the UV and IR, with a_2 and a_4 weights respectively. The a_1 parameter accounts for contributions to the refractive index from plasmons in the far UV, whereas a_6 accounts for phonon absorptions in the far IR. The b_i parameters account for thermal effects, involving the temperature dependent parameter f, which is given by

$$f(T) = (T - T_0)(T + T_0 + 2 \times 273.16) \tag{A.6}$$

$$= (T - 24.5)(T + 570.82) \tag{A.7}$$

Parameters	MgO:PPLN	
	n_e	n_o
a_1	5.756	5.653
a_2	0.0983	0.1185
a_3	0.2020	0.2091
a_4	189.32	89.61
a_5	12.52	10.85
a_6	1.32×10^{-2}	1.97×10^{-2}
b_1	2.860×10^{-6}	7.941×10^{-7}
b_2	4.700×10^{-8}	3.134×10^{-8}
b_3	6.113×10^{-8}	-4.641×10^{-9}
b_4	1.516×10^{-4}	-2.188×10^{-6}

Table A.5: Sellmeier coefficients for 5 % MgO doped congruent lithium niobate (MgO:PPLN).

B Statistical Error

Assuming a poissonian probability distribution, the statistical error of the measured coincidence rates is

$$\Delta N_{ij} = \sqrt{N_{ij}} \tag{B.1}$$

For example, the error ΔP_{HH} of the calculated probability P_{HH} is

$$\Delta P_{HH} = \sqrt{\left(\frac{N_s - N_{HH}}{N_s^2}\Delta N_{HH}\right)^2 + \left(\frac{N_{VH}}{N_s^2}\Delta N_{HV}\right)^2 + \left(\frac{N_{HH}}{N_s^2}\Delta N_{VH}\right)^2 + \left(\frac{N_{HH}}{N_s^2}\Delta N_{VV}\right)^2} \tag{B.2}$$

where $N_s = N_{HH} + N_{VV} + N_{VH} + N_{HV}$ is the sum of all counts in the chosen basis.

B.1 Visibility

The statistical error of the visibility $V = \frac{N_{HH}-N_{HV}}{N_{HH}+N_{HV}}$ is

$$\Delta V = \sqrt{\frac{1}{N_s}\left(1 - V^2\right)} \tag{B.3}$$

whith N_s defined as $N_s = H_{HH} + N_{HV}$.

B.2 Bell-state Fidelity

For the statistical error of the Bell-state fidelity F follows:

$$\Delta F = \frac{1}{2}\sqrt{(\Delta P_{HH})^2 + (\Delta P_{VV})^2 + (\Delta P_{DD})^2 + (\Delta P_{AA})^2 + (\Delta P_{RR})^2 + (\Delta P_{LL})^2} \tag{B.4}$$

B.3 Entanglement Witness

For the statistical error of the entanglement witness W follows:

$$\Delta W = \frac{1}{2}\sqrt{(\Delta P_{HV})^2 + (\Delta P_{VH})^2 + (\Delta P_{DD})^2 + (\Delta P_{AA})^2 + (\Delta P_{RR})^2 + (\Delta P_{LL})^2} \tag{B.5}$$

Selbständigkeitserklärung

Hiermit versichere ich, dass ich die vorliegende Arbeit selbständig verfasst und keine anderen als die angegebenen Quellen und Hilfsmittel verwendet habe.

Thomas Kreißl Berlin, den 31.03.2015